

**Innovations of wide-field optical-sectioning fluorescence
microscopy: toward high-speed volumetric bio-imaging with
simplicity**

Thesis by

Jiun-Yann Yu

In Partial Fulfillment of the Requirements

for the Degree of

Doctor of Philosophy



California Institute of Technology

Pasadena, California

2014

(Defended March 25, 2014)

© 2014

Jiun-Yann Yu

All Rights Reserved

Acknowledgements

Firstly, I would like to thank my thesis advisor, Professor Chin-Lin Guo, for all of his kind advice and generous financial support during these five years. I would also like to thank all of the faculties in my thesis committee: Professor Geoffrey A. Blake, Professor Scott E. Fraser, and Professor Changhui Yang, for their guidance on my way towards becoming a scientist. I would like to specifically thank Professor Blake, and his graduate student, Dr. Daniel B. Holland, for their endless kindness, enthusiasms and encouragements with our collaborations, without which there would be no more than 10 pages left in this thesis. Dr. Thai Truong of Prof. Fraser's group and Marco A. Allodi of Professor Blake's group are also sincerely acknowledged for contributing to this collaboration.

All of the members of Professor Guo's group at Caltech are gratefully acknowledged. I would like to thank our former postdoctoral scholar Dr. Yenyu Chen for generously teaching me all the engineering skills I need, and passing to me his pursuit of wide-field optical-sectioning microscopy. I also thank Dr. Mingxing Ouyang for introducing me the basic concepts of cell biology and showing me the basic techniques of cell-biology experiments. I would like to pay my gratefulness to our administrative assistant, Lilian Porter, not only for her help on administrative procedures, but also for her advice and encouragement on my academic career in the future.

Here I thank Dr. Ruben Zadoyan and his former group member Dr. Chun-Hung Kuo for our collaboration on the project of diffuser-based temporal focusing. I would like to thank Professor Young-Geun Han and his group members Sunduck Kim and Young Bo Shim at Hanyang University who made the fiber-illumination project possible. Professor Wonhee Lee and his group member Jonghyun Kim at Korea Advanced Institute of Science and Technology are gratefully acknowledged for developing the prototype of the height-staggered plates. My sincere acknowledgment also goes to

Professor Paul Sternberg and his group member Hui Chiu, who kindly helped me prepared *C. elegans* of several different lines for imaging. Meanwhile, I would like to thank Dr. Chao-Yuan Yeh for his advice on choosing appropriate biological samples, and Yun Mou for his advice on using appropriate fluorescent dyes that facilitated axial response measurements. Special thanks to my friends Yu-Hang Chen for his assistance in computation, and Dr. Chien-Cheng Chen for his inspiring suggestions on my research works.

I would like to acknowledge Dr. Alexander Egner for his inspiring instructions with the theoretical calculations in this Thesis. I can't thank Professor Shi-Wei Chu at National Taiwan University enough for training me with the basic knowledge and experimental skills of imaging optics, and helping me pave the way to continue my research of optical microscopy at Caltech. I thank Professor Carol J. Cogswell at University of Colorado, Boulder for being a role model for me and for encouraging me to continue my research approach in developing simple, useful, and cost-efficient microscopy techniques.

I sincerely acknowledge all of the administrative staffs of Bioengineering option, especially Linda Scott, for helping me with all the administrative procedures during these years.

I would like to specifically thank my friends Yun Mou, Dr. Chao-Yuan Yeh and Mike (Miroslav) Vondrus, for their company and endless support on good days and bad days. I gratefully thank Chan U Lei, Tong Chen, Hao Chu, Hui-Chen Chen, Myoung-Gyun Suh, Wai Chung Wong, Hsiu-Ping Lee, and Tzu-Chin Chen for our friendship.

There are no words that I can find to express my thankfulness properly to my parents, Jen-Hui Hsieh and An-Chi Yu; they supported me with no hesitations and no matter how far I deviated from the route they planned for me. I also thank my sister Chao-Wei Yu and my brother-in-law Bei-Jiang Lin for their warm, continuing greetings during my good times and bad times, and I wish that their newborn baby, also my nephew, Tzu-Yang Lin, have a wonderful adventure of life ahead of him. At last, I would like to acknowledge Wen-Hsuan Chan, who had been my strongest support in the past ten years.

Abstract

Optical microscopy has become an indispensable tool for biological researches since its invention, mostly owing to its sub-cellular spatial resolutions, non-invasiveness, instrumental simplicity, and the intuitive observations it provides. Nonetheless, obtaining reliable, quantitative spatial information from conventional wide-field optical microscopy is not always intuitive as it appears to be. This is because in the acquired images of optical microscopy the information about out-of-focus regions is spatially blurred and mixed with in-focus information. In other words, conventional wide-field optical microscopy transforms the three-dimensional spatial information, or volumetric information about the objects into a two-dimensional form in each acquired image, and therefore distorts the spatial information about the object. Several fluorescence holography-based methods have demonstrated the ability to obtain three-dimensional information about the objects, but these methods generally rely on decomposing stereoscopic visualizations to extract volumetric information and are unable to resolve complex 3-dimensional structures such as a multi-layer sphere.

The concept of optical-sectioning techniques, on the other hand, is to detect only two-dimensional information about an object at each acquisition. Specifically, each image obtained by optical-sectioning techniques contains mainly the information about an optically thin layer inside the object, as if only a thin histological section is being observed at a time. Using such a methodology, obtaining undistorted volumetric information about the object simply requires taking images of the object at sequential depths.

Among existing methods of obtaining volumetric information, the practicability of optical sectioning has made it the most commonly used and most powerful one in biological science. However, when applied to imaging living biological systems, conventional single-point-scanning optical-sectioning

techniques often result in certain degrees of photo-damages because of the high focal intensity at the scanning point. In order to overcome such an issue, several wide-field optical-sectioning techniques have been proposed and demonstrated, although not without introducing new limitations and compromises such as low signal-to-background ratios and reduced axial resolutions. As a result, single-point-scanning optical-sectioning techniques remain the most widely used instrumentations for volumetric imaging of living biological systems to date.

In order to develop wide-field optical-sectioning techniques that has equivalent optical performance as single-point-scanning ones, this thesis first introduces the mechanisms and limitations of existing wide-field optical-sectioning techniques, and then brings in our innovations that aim to overcome these limitations. We demonstrate, theoretically and experimentally, that our proposed wide-field optical-sectioning techniques can achieve diffraction-limited optical sectioning, low out-of-focus excitation and high-frame-rate imaging in living biological systems. In addition to such imaging capabilities, our proposed techniques can be instrumentally simple and economic, and are straightforward for implementation on conventional wide-field microscopes. These advantages together show the potential of our innovations to be widely used for high-speed, volumetric fluorescence imaging of living biological systems.

Contents

Acknowledgements	iii
Abstract	v
1 Introduction: the roles of optical sectioning and fluorescence imaging in biological researches	1
1.1 Image formation in a far-field optical imaging system	5
2 Optical sectioning	10
2.1 Single-point-scanning optical sectioning: confocal and multiphoton excitation fluorescence microscopy	10
2.1.1 Mechanism	10
2.1.2 Discussions	11
2.2 Existing methods for wide-field optical sectioning	12
2.2.1 Multifocal confocal microscopy and (time-multiplexed) multifocal multiphoton microscopy	12
2.2.2 Structured illumination microscopy	13
2.2.3 Temporal focusing	14
2.2.4 Selective plane illumination microscopy (SPIM)	15
2.2.5 Brief summary	15
3 New methods for wide-field optical sectioning microscopy	16

3.1	Diffuser-based temporal focusing microscopy: generating temporal focusing without high-order diffraction	16
3.1.1	Theoretical estimations	18
3.1.2	Methods and Materials	24
3.1.3	Results	25
3.1.4	Discussion	27
3.1.5	Brief summary	32
3.2	Temporal focusing or dense time multiplexing by height-staggered microlens array	32
3.2.1	Design of a HSMA-based temporal focusing microscope	34
3.2.2	Construct a physical optics-based model taking into account temporal interferences	37
3.2.3	Optimize optical sectioning through tuning N_t and δt	39
3.2.4	Experimental verification of reduction of out-of-focus excitation by HSMA	42
3.2.5	Enhance optical sectioning by implementing structured illumination microscopy	45
3.2.6	Brief summary	51
3.3	High-degree time-multiplexed multifocal multiphoton microscopy by a length-staggered fiber bundle	51
3.3.1	Fiber bundle manufacturing	59
3.3.2	Statistical analysis of the degree of time multiplexing	60
3.3.3	Development of the optical system	60
3.3.4	Measurement of axial responses	61
3.3.5	Estimating the upper bound of the number of unique time delays	62
4	Discussions and Conclusions	63
4.1	Discussions	63
4.2	Conclusions	64
	Bibliography	67

Chapter 1

Introduction: the roles of optical sectioning and fluorescence imaging in biological researches

Far-field optical microscopy is arguably the most important imaging tool for biological science. It features 1) non-invasive and non-destructive observations using visible, near-infrared and near-ultraviolet light, 2) sub-cellular spatial resolutions and sub-millisecond temporal resolution, 3) simple requirements for instrumentation and laboratory environment, and 4) delivering intuitive, pictorial information about the observed objects.

Nonetheless, the spatial information provided by conventional far-field optical imaging methods is not always considered quantitatively accurate even the desired spatial resolution is below the axial resolution of the imaging system. This is because the 2-dimensional pictorial information acquired by array detectors or films of the imaging systems is actually a mixture of 3-dimensional information about the objects, as revealed in the following Section. In Section 1.1 we will see that when a 3-dimensional object is uniformly illuminated, the image forms at the plane of the detector array is 3-dimensional convolution of the spatial information about the object with the point spread function of the imaging system. It is theoretically possible to deconvolve a stack of images obtained at sequential depths with the point spread function of the imaging system to retrieve the volumetric information about the objects. Using such an approach, the fidelity of the processed volumetric information largely relies on high-signal-to-noise ratio imaging as well as the objects' structural sparsity and/or simplicity. Nonetheless, when the structure of the observed object is complex (i.e.,

not a few points or lines) and/or the signal-to-noise ratio of the obtained images is low, both of which are frequently encountered situations when imaging fluorescent protein-labeled molecules in living cells and tissues.

A centuries-old method to prevent the aforementioned dimension-mixing issue is histological sectioning, i.e., slicing the objects into a series of thin layers. If the thickness of each slice is thinner than or as thin as the depth of field of the imaging system, each slice is then an optically 2-dimensional object and thus the information obtained from an array detector can be considered quantitatively accurate at the spatial resolution of the imaging system. However, such a method is not applicable if the dynamics of biological systems are of interest.

Optical sectioning [1, 2, 3, 4, 5, 6, 7], alternatively, are optical imaging techniques that detect the light emitted or scattered mainly from an optically thin layer at each acquisition, so that the pictorial information obtained from the array detector, as if in the case of histological sectioning, can be considered quantitatively accurate at the spatial resolution of the imaging system. Based on this imaging mechanism, to build up volumetric information using optical-sectioning techniques requires only acquiring a stack of images at sequential depths inside the object. Further discussion about various methods of optical sectioning can be found in Chapter 2. Beside optical sectioning, fluorescence holography [8, 9, 10] and certain quantitative phase imaging methods [11] can also be used to obtain certain volumetric information of objects. Nonetheless, these techniques typically presume certain interference conditions to retrieve the volumetric information and thus are limitedly applicable for bio-imaging. To date, optical sectioning remains the most widely used method to obtain volumetric information about microscopic objects in biological and biomedical studies owing to its broad applicability.

The source of contrasts is also an important perspective of optical microscopy. Commonly used contrasts include absorption, scattering, phase contrast [12], coherence, polarization, reflection, spectral response, fluorescence and etc.; there are also integrated imaging techniques utilizing the mixture of several sources of contrasts for specific imaging tasks. The choice of image contrasts mostly depends on the optical properties of investigated biological materials/phenomena. Among

these, dye-based spectral absorption and fluorescence are of particular interests to biologists and biochemists because chemical dyes have been successfully engineered to attach to specific types of molecules and thus the acquired images provide spatial information associated with chemical components. In particular, the discovery of green fluorescent protein and successful development of genetic methods for attaching it to specific gene-expressed molecules [13] made it possible for biologists to engineer fluorescent probes for almost any bio-molecules of interest without the concern of toxicity, which are frequently found in organic dyes. Such a feature greatly facilitates the observations of spatial-temporal molecular dynamics in biological systems, and fluorescence ever since became an increasingly important source of image contrast. There are also ongoing studies investigating more delicate biological activities than molecule localization using fluorescence-based image contrasts, such as fluorescence-lifetime imaging microscopy [14] and Förster resonance energy transfer microscopy [15].

The versatility of fluorescent protein-based probes and the capability of obtaining accurate spatial information of optical-sectioning techniques together explain the broad practices of optical-sectioning fluorescence microscopy to investigate the most challenging issues in nowadays biological and biomedical researches. While biologists and biochemists have been exploring new possibilities of fluorescent proteins during the past two decades, the limitations of existing optical-sectioning techniques, on the other hand, posed more and more practical difficulties. Confocal fluorescence microscopy and multiphoton excitation fluorescence microscopy, both the gold standards of optical-sectioning techniques, are known to be either slow in imaging speed or deleterious to living biological systems [1, 16, 17]. Another issue of these two techniques is the engineering complexity of the optical systems, which results in the high market prices of commercial systems and prevents broad access of these instrumentations. Such issues, as we later discuss in Section 2.1, mainly raise from the single-point-scanning mechanism of these two techniques. In the past two decades there have been several wide-field optical-sectioning techniques proposed and demonstrated to overcome the limitations of single-point-scanning optical-sectioning methods. However, as we will see in Section 2.2, most of the proposed wide-field optical-sectioning techniques provide quite limited improvements and/or bring

in new limitations. As a result, confocal and multiphoton excitation fluorescence microscopy remain the most commonly used optical-sectioning techniques even for imaging living biological systems.

To overcome the aforementioned issues of existing optical-sectioning fluorescence microscopy techniques, this thesis aims at 1) to understand the advantages and limitations of existing optical-sectioning fluorescence microscopy, with a special interest in wide-field optical sectioning for its suitability for observing living biological systems, and 2) to propose new modifications and methods to overcome the limitations of existing techniques encountered in bio-imaging applications, and 3) to do so with simplicity of the optical system as well as operation procedures. In the following section, we briefly go through the principles of image formation in conventional far-field imaging systems and establish the theoretical bases and terminology that are used for the rest of this thesis. Chapter 2 then discusses the mechanisms of individual existing optical-sectioning techniques, including both single-point-scanning and wide-field approaches. At the end of Chapter 2, we discuss the disadvantages and limitations of existing optical-sectioning techniques. Chapter 3 brings in the innovations we made to overcome the limitations of existing techniques: our methods integrate existing wide-field optical-sectioning techniques and utilize their advantages to compensate the disadvantages of one another. I also introduce how to quantitatively estimate the optical characteristics of our techniques, on the basis of physical optics, for system optimization. Although our proposed integrated system surpasses most of existing wide-field optical-sectioning techniques, it is subject to exactly the same fundamental limitation of those techniques in terms of reducing out-of-focus excitation by introducing time delays. With this regard, in the last section of Chapter 3, we demonstrate a novel design of illumination device that can fundamentally resolve this limitation and achieve the same optical-sectioning capability of single-point-scanning multiphoton excitation fluorescence microscopy. The last chapter discusses possible strategies to optimize our proposed techniques, and provide a comprehensive comparison of existing optical-sectioning techniques.

1.1 Image formation in a far-field optical imaging system

This section describes the basic principles of image formation in a far-field optical imaging system on the basis of physical optics. More details of this topic can be found in several widely referenced microscopy-related literatures such as references [18, 19], and the purpose of this section is mainly for brief introduction and to develop the terminology frequently used in this thesis.

For the convenience of theoretical treatment, we consider that a typical far-field imaging system consists of three parts: an object, imaging optics, and the object image formed on an photosensitive array detector (typically a camera, Fig. 1.1). At the object, we consider the component of emitted electromagnetic field of wavenumber k as $E_{\text{obj}}(k, x, y, z, t) e^{i(\omega t + \delta\theta(k, x, y, z, t))}$. Here $E_{\text{obj}}(k, x, y, z, t)$ is the scalar amplitude of the field, and we assume that its temporal variation is much slower than optical frequency. ω is the angular frequency of the electromagnetic wave and is defined as $c k$, where c is the speed of light; $\delta\theta$ is a randomized phase shift representing the incoherent component of the the electromagnetic wave. The imaging optics can be characterized by its amplitude point spread function $E_{\text{PSF}}(k, x, y, z, x', y')$, which describes the electromagnetic field at the image plane (Camera in Fig. 1.1) contributed by an coherent ideal point source of wavenumber k at (x, y, z) . E_{PSF} should be, in general, a function of z' , which is omitted here because in most far-field imaging systems the camera is fixed at a certain depth and therefore z' is a constant. For a translation-invariant optical system, we can reduce the amplitude point spread function to $E_{\text{PSF}}(k, x' - Mx, y' - My, M^2 z)$, where M is the magnification of the imaging system. This is a practical approximation for well-corrected microscope objectives used in modern biomedical microscopy systems [18]. It should be noted that the sign of M is determined by the orientation of image relative to the object: M is negative for an inverse-imaging system and is positive for an upright-imaging system. Now we can write down the electromagnetic field at the camera, or, the object (amplitude) image of wavenumber k , as:

$$\begin{aligned}
 & E_{\text{img}}(k, x', y', t) \\
 &= \int_X \int_Y \int_Z E_{\text{PSF}}(k, x' - Mx, y' - My, M^2 z) E_{\text{obj}}(k, x, y, z, t) e^{i(\omega t + \delta\theta(k, x, y, z, t))} dx dy dz, \quad (1.1)
 \end{aligned}$$

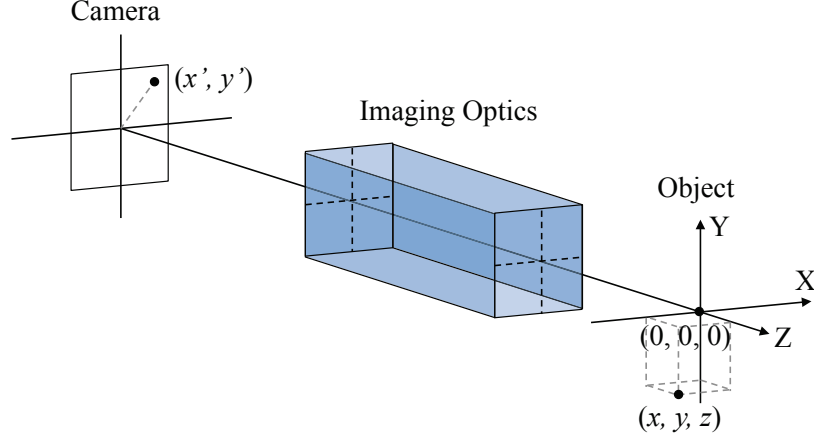


Figure 1.1: Scheme of a typical far-field imaging system

or simply:

$$E_{\text{img}} = E_{\text{PSF}} \otimes_{X,Y,Z} E_{\text{obj}}, \quad (1.2)$$

indicating that the field profile at the image plane is a three-dimensional convolution (in X, Y, Z) of the amplitude object and the amplitude point spread function of the imaging system [18, 19].

The camera, or the array detector, detects the intensity distribution, i.e., $|E_{\text{img}}^2|$, at the image plane. The signal collected by a unit detector, commonly referred to as a 'pixel,' is the integral of intensity over the pixel area and exposure time [18, 19]; 'photon counts' is commonly used as the unit of such signals. For simplicity, we can consider that the camera is an array of infinitesimal pixels, which allows us to omit the spatial integrations, and the signal per unit area collected by a pixel at (x', y') at time t_1 within an exposure time δt can be written as:

$$\begin{aligned} I_{\text{img}}(k, x', y', t_1, \delta t) &= \int_{t_1}^{t_1 + \delta t} |E_{\text{img}}(k, x', y', t)|^2 dt \\ &= \int_{t_1}^{t_1 + \delta t} E_{\text{img}}(k, x', y', t) \cdot E_{\text{img}}^*(k, x', y', t) dt \\ &= \int_{t_1}^{t_1 + \delta t} \int_{X_a, Y_a, Z_a, X_b, Y_b, Z_b} E_{\text{PSF}}(k, x' - Mx_a, y' - My_a, M^2 z_a) E_{\text{PSF}}^*(k, x' - Mx_b, y' - My_b, M^2 z_b) \\ &\quad \times E_{\text{obj}}(k, x_a, y_a, z_a, t) E_{\text{obj}}^*(k, x_b, y_b, z_b, t) \\ &\quad \times e^{i(\delta\theta(k, x_a, y_a, z_a, t) - \delta\theta(k, x_b, y_b, z_b, t))} dx_a dy_a dz_a dx_b dy_b dz_b dt. \end{aligned} \quad (1.3)$$

Now if we assume that 1) the variation of E_{obj} in time is slow enough to be negligible during a δt period, and 2) the electromagnetic field emitted at the object is spatially incoherent because the coherent length is much smaller than the finest feature that can be resolved by the imaging system, which is generally applicable to fluorescence imaging, we have:

$$\begin{aligned} & \int_{t_1}^{t_1+\delta t} E_{\text{obj}}(k, x_a, y_a, z_a, t) E_{\text{obj}}^*(k, x_b, y_b, z_b, t) e^{i(\delta\theta(k, x_a, y_a, z_a, t) - \delta\theta(k, x_b, y_b, z_b, t))} dt \\ & \approx \delta t E_{\text{obj}}(k, x_a, y_a, z_a, t_1) E_{\text{obj}}^*(k, x_b, y_b, z_b, t_1) \delta(x_1 - x_2, y_1 - y_2, z_1 - z_2). \end{aligned} \quad (1.4)$$

Combining eqs. 1.3 and 1.4 we derive:

$$\begin{aligned} & I_{\text{img}}(k, x', y', t_1, \delta t) \\ & \approx \delta t \int_{X_a, Y_a, Z_a, X_b, Y_b, Z_b} E_{\text{PSF}}(k, x' - Mx_a, y' - My_a, M^2 z_a) E_{\text{PSF}}^*(k, x' - Mx_b, y' - My_b, M^2 z_b) \\ & \quad \times E_{\text{obj}}(k, x_a, y_a, z_a, t_1) E_{\text{obj}}^*(k, x_b, y_b, z_b, t_1) \delta(x_a - x_b, y_a - y_b, z_a - z_b) dx_a dy_a dz_a dx_b dy_b dz_b \\ & = \delta t \int_{X, Y, Z} |E_{\text{PSF}}(k, x' - Mx, y' - My, M^2 z)|^2 |E_{\text{obj}}(k, x, y, z, t_1)|^2 dx dy dz \\ & = \delta t \int_{X, Y, Z} I_{\text{PSF}}(k, x' - Mx, y' - My, M^2 z) I_{\text{obj}}(k, x, y, z, t_1) dx dy dz \\ & = \delta t I_{\text{PSF}} \otimes_{X, Y, Z} I_{\text{obj}}, \end{aligned} \quad (1.5)$$

where I_{PSF} and I_{obj} respectively denote the intensity point spread function of the imaging optics and the intensity profile of the object. Equation 1.5 shows us that when the electromagnetic field emitted at the object is spatially incoherent, the image acquired by the camera is simply the convolution of the intensity profile at the object and the intensity point spread function of imaging optics.

An important message we learn from eqs. 1.3 and 1.5 is that the 2-dimensional information provided by the acquired image is actually a mixture of 3-dimensional information about the object, which is now expressed explicitly as the 3-dimensional (X, Y, Z) convolution. Considering such a dimension mixing and reduction process of image formation in an far-field imaging system, we can realize that the acquired images does not provide reliable quantitative information about the object even at the spatial resolutions of the imaging system. We can use a simple object, a constantly

bright point source at $(0, 0, z_0)$, to visualize such an issue. To calculate the image of this object, we simply substitute $\delta(x, y, z - z_0)$ for I_{obj} in eq. 1.5 so that:

$$\begin{aligned} I_{\text{img}}(k, x', y') &= \int_{X,Y,Z} I_{\text{PSF}}(k, x' - Mx, y' - My, M^2z) \delta(x, y, z - z_0) dx dy dz \\ &= I_{\text{PSF}}(k, x', y', M^2z_0). \end{aligned} \quad (1.6)$$

Here we can omit time-related terms as long as the point source is assumed to have a constant brightness. To simplify the math, we assume the point spread function is in the form of a 00-mode Gaussian beam so that:

$$I_{\text{img}}(k, x', y') = I_0 \left(\frac{w_0}{w(M^2z_0)} \right)^2 \exp \left(\frac{-2(x'^2 + y'^2)}{w(M^2z_0)^2} \right), \quad (1.7)$$

where:

$$w(z) = w_0 \sqrt{1 + \frac{z\lambda}{\pi w_0^2}}. \quad (1.8)$$

Equation 1.7 suggests that the image of a point source is a 2-dimensional Gaussian distribution wherein the width of the distribution is a function of z_0 . A feature of conventional far-field imaging revealed by eq. 1.7 is that the total signal collected by the array detector is more or less the same no matter what the depth of the point source is. We can verify this feature simply by integrating I_{img} over x' and y' :

$$\begin{aligned} &\int_{-\infty}^{\infty} \int_{-\infty}^{\infty} I_{\text{img}} dx' dy' \\ &= I_0 \left(\frac{w_0}{w(M^2z_0)} \right)^2 \int_{-\infty}^{\infty} \int_{-\infty}^{\infty} \exp \left(\frac{-2(x'^2 + y'^2)}{w(M^2z_0)^2} \right)^2 dx' dy' \\ &= I_0 \left(\frac{w_0}{w(M^2z_0)} \right)^2 \times \pi \frac{w(M^2z_0)^2}{2} = \pi I_0 w_0^2/2, \end{aligned} \quad (1.9)$$

and the result shows no dependence on z_0 . Such a feature indicates that, when imaging a thick sample, the signals coming from different depths, in terms of photon counts, have nearly equal contributions to the acquired image. Noteworthy, the integral of signals obtained by the detector

as a function of the depth of a point source, as exemplified by eq. 1.9, is commonly referred to as axial response. Axial response is frequently used to quantify the capability of optical sectioning of an optical imaging system, and its full width at half maximum (FWHM) is typically defined as the axial resolution of an optical-sectioning imaging system.

Theoretically it is possible to deconvolve a stack of images acquired at sequential depths with the intensity point spread function to retrieve accurate spatial information about the object. Such a method, however, is limitedly applied to biologically relevant imaging tasks because the fidelity of the results of deconvolution demands sparsity of light-emitting sources in the object and high signal-to-noise ratios of acquired images, which are not always satisfied in biological imaging and especially not so when high-frame-rate imaging of fluorescent proteins is required.

Optical sectioning, on the other hand, takes a totally different approach to retrieve 3-dimensional spatial information about the object. The main concept of optical sectioning is to manipulate the axial response of an optical imaging system such that the maximal response occurs at the depth where the I_{PSF} has the narrowest lateral distribution. In certain types of optical-sectioning techniques the signal coming from outside of half maximums of axial response can be considered negligible, which makes the obtained spatial information accurate as long as the required axial and lateral resolutions are not finer than the full widths at half maximums of axial response and lateral point spread function of the imaging system. In the next chapter we discuss several optical-sectioning techniques and their optical properties.

Chapter 2

Optical sectioning

2.1 Single-point-scanning optical sectioning: confocal and multiphoton excitation fluorescence microscopy

2.1.1 Mechanism

Conventional confocal fluorescence microscopy and multiphoton excitation fluorescence microscopy, although share similar optical designs and instrumentations [1, 2], achieve optical sectioning through completely different mechanisms. Confocal fluorescence microscopy tightly focuses a beam onto the object, and positions a pinhole or a small aperture at the conjugate point of the focal spot in front of a photodetector [1, 20]. With such a geometrical arrangement, the pinhole allows most of focal-spot emission going through while blocking most of emission outside of the focal spot, and thus achieve optical sectioning. The axial response at out-of-focus region can be straightforwardly derived as $1/z^2$ on the basis of geometrical optics. Rigorous derivations of the axial response of confocal fluorescence microscopy, which convolves the focused beam profile with a modified I_{PSF} containing a pupil function to describe the pinhole, can be found in reference [20].

Multiphoton excitation fluorescence microscopy, on the other hand, utilizes the nonlinear excitation efficiency to create optical sectioning [2]. For simplicity, we can again assume the focused beam

profile to be a 00-mode Gaussian beam, and, for 2-photon excitation, the axial response is:

$$\int_{X,Y} \left(I_0 \left(\frac{w_0}{w(z)} \right)^2 \exp \left(\frac{-2(x^2 + y^2)}{w(z)^2} \right) \right)^2 dx dy \propto \frac{1}{w(z)^2}. \quad (2.1)$$

From eq. 1.8 we can see that the axial response of two-photon excitation fluorescence microscopy is approximately proportional to $1/z^2$ at out-of-focus regions. Alternatively, one can derive this $1/z^2$ out-of-focus response on the basis of geometrical optics, just as in the case of confocal fluorescence microscopy.

2.1.2 Discussions

The $1/z^2$ axial response at out-of-focus regions in confocal and two-photon excitation fluorescence microscopy is now the gold standard of optical-sectioning techniques. Nonetheless, the single-point-scanning mechanism of these two techniques raises certain issues and limitations in bio-imaging applications. Unlike conventional far-field optical image formation, the pixel-by-pixel signal acquisition of single-point-scanning mechanism drastically slows down the imaging speeds and complicates the instrumentations. Meanwhile, to obtain images at reasonable frame rates, the dwell time of the focal point at each pixel has to be short enough (typically from sub- μ s to 100 μ s), and thus requires high focal intensity (typically $> 10^5$ times higher than in conventional wide-field fluorescence microscopy) for sufficient fluorescence emission. Such high focal intensity, however, has been found to result in various photo-damages in living biological systems. Indeed, photo-toxicity in the scanned live organisms has been frequently observed during video-rate time-lapse imaging on conventional confocal microscopes [1]. Although such photo-toxicity can be greatly reduced by using multi-photon excitation fluorescence microscopy [16, 21], a tradeoff is the thermal mechanical damage to living tissues through the single-photon absorption of its near-infrared excitation [17].

An alternative approach to resolve photo/thermal-damages in conventional single-point-scanning optical-sectioning microscopies without significant losses of acquisition speed is to implement the capability of optical sectioning in wide-field optical microscopy. The wide-field microscopy techniques

mentioned here and hereafter in this thesis refer to those techniques wherein the image formation is accomplished mainly by optical far-field imaging, and does not require *a priori* knowledge of spatial-temporal information of illumination. In the next section we discuss several existing methods for wide-field optical-sectioning microscopy including multifocal multiphoton microscopy, structured illumination microscopy, temporal focusing, and selective plane illumination microscopy [7, 3, 5, 22, 6].

2.2 Existing methods for wide-field optical sectioning

2.2.1 Multifocal confocal microscopy and (time-multiplexed) multifocal multiphoton microscopy

The concept of multifocal confocal microscopy and multifocal multiphoton microscopy is to have multiple channels that excite and detect the fluorescence signal coming from the object in a temporally parallel manner [23, 4], so as to speed up the image formation process. In these techniques, multiple foci are created as independent channels for excitation in and detection from the sample.

To preserve the capability of optical sectioning, however, the spatial distribution of foci has to be sufficiently sparse, which limits the degree of parallelization. This is because signal crosstalk among parallel channels in multifocal confocal microscopy and out-of-focus excitation in multifocal multiphoton microscopy become significant as the interfocal distances of the foci decrease. Take an oil-immersion NA 1.42 objective lens for example, the distance between neighboring foci d_{foci} that preserves the $1/z^2$ axial response at out-of-focus regions is approximately 5 times of the excitation wavelength λ [5], while the diameter of the focal spots f_0 is approximately 0.3λ , which makes the fraction of un-illuminated area approximately $1 - (\frac{d_{\text{foci}}}{d_0})^2 \approx 99.6\%$. Such a high fraction of un-illuminated area requires a large number of scanning steps to illuminate the entire field of view, and thus greatly limit the improvements of imaging speed in multifocal confocal/multiphoton microscopy.

To cover the un-illuminated area, Egner et al. [5] proposed to use time multiplexing, i.e., generating multiple foci that are largely separated in time, so that the interferences among these foci

is negligible even though they partially overlap in space. The number of distinct time-delay steps required to cover the un-illuminated area, N_t , can be estimated as

$$N_t \approx \left(\frac{d_0}{d_{\text{foci}}}\right)^2 \approx 280. \quad (2.2)$$

Nonetheless, due to the difficulties of fabricating the temporal delay mask, an optical element that has large numbers of distinct height levels on its surface, the number of distinct time delays practically achieved to date through this approach is only 3. We further discuss the details about the fabrication of temporal delay masks in Section 3.2 and 3.3.

2.2.2 Structured illumination microscopy

In contrast to multifocal confocal/multiphoton microscopy, structured illumination is a much more successful example of achieving wide-field optical sectioning in terms of system complexity and imaging speeds. The working principle of structured illumination microscopy is a fundamental property of incoherent far-field imaging: higher spatial frequency components of the images decay more rapidly with defocusing. Structured illumination microscopy illuminates the object with a high-spatial-frequency excitation pattern and acquires several images with the excitation pattern translated to different positions. Then a simple algorithm that filters high-spatial-frequency components is applied to extract the in-focus fluorescence signal. Reference [3] shows, theoretically and experimentally, that structured illumination microscopy shares a similar axial response as conventional confocal microscopy.

However, the single-photon excitation of conventional structured illumination microscopy excites the full depth of the sample within the field of view - an extremely inefficient use of the quantum yield of the fluorophores that can lead to significant photobleaching in a thick object as found in confocal microscopy. Also, at each acquisition, structured illumination microscopy receives fluorescence over a full depth range and numerically removes most of it afterward. Such a procedure can sacrifice the dynamic range of the camera for unwanted (out-of-focus) information and result in degraded

signal-to-noise ratios of the processed images.

2.2.3 Temporal focusing

Temporal focusing is a multiphoton excitation-based technique that inherits the concept of time-multiplexed multifocal multiphoton microscopy: introducing time delays to reduce out-of-focus excitation [6]. In temporal focusing, a light-scattering plate creates continuous time delays (in contrast to multiple discrete time delays in time-multiplexed multifocal multiphoton microscopy). Instead of forming a group of temporally separated foci, the net effect of such continuous time delays is that the effective pulse duration of the excitation light pulses varies as the pulse propagates along the optical axis, and is shortest at the conjugate plane of the light-scattering plate. Owing to the nonlinear excitation efficiency of multiphoton excitation, the higher peak intensity associates with a shorter pulse duration, which provides the optical-sectioning effect. Temporal focusing microscopy was first experimentally demonstrated by Oron et al. [6]. In their setup, the laser pulse is directed to a blazed grating, which serves as the light-scattering plate, in an oblique incidence orientation. The illustration of the time course of temporal focusing resembles conventional multiphoton line-scan mechanism. A geometry-based model can be used to estimate the effective pulse duration and as a function of depth [6] and hence the optical-sectioning effect.

However, this implementation of temporal focusing relies on high-order diffracted beams for excitation, and therefore the optical path of the system depends on the wavelength of the excitation light. If one uses an ultrafast oscillator with a wavelength-tunable output as the excitation light source, it is technically possible to build a mechanical arm system that can rotate and translate a mirror to suit various wavelengths, but such an optical design is not practically favorable, and it does not work for multiple excitations at the same time. As a result, temporal focusing is inconvenient when multiple excitation wavelengths are required for imaging, which is frequently encountered in bio-imaging tasks such as investigating the spatial-temporal correlations of two or more bio-molecules in the specimen.

2.2.4 Selective plane illumination microscopy (SPIM)

Unlike most of the aforementioned techniques that use a single microscope objective for both illumination and detection, selective plane illumination microscopy requires an additional illumination path orthogonal to the detection path to deliver a sheet-like excitation profile [7, 24]. Recently, this technique has been found particularly useful to observe cell motions during embryonic development [7, 25].

However, the illumination mechanism of SPIM leads to a tradeoff between the size of the field of view and axial resolution. This tradeoff results from the nature of diffraction of light: the smaller the focal spot (or beam waist), the faster the beam converges and diverges, and thus the shorter depth of focus. For example, if a $1\text{-}\mu\text{m}$ axial resolution is required, the width of field of view, i.e., the depth of focus of the illumination beam, would be no larger than $10\ \mu\text{m}$ [26]. In addition, the close proximity of separate illumination and imaging optics in SPIM raises the system complexity considerably and can lead to sample-handling difficulties.

2.2.5 Brief summary

In summary, currently existing wide-field optical-sectioning techniques still have their own issues in bio-imaging applications. These techniques may be useful for certain imaging tasks, but for general bio-imaging purposes, single-point-scanning confocal and multiphoton excitation fluorescence microscopy remains the most commonly used optical-sectioning methods, and this is true even for imaging living biological systems. In this regard, the next chapter discusses the innovations we made based on integrating existing techniques to compensate the drawbacks of one another; we demonstrate that our proposed wide-field optical-sectioning imaging technique have a simple optical design with optical performance equivalent to or better than single-point-scanning optical sectioning techniques.

Chapter 3

New methods for wide-field optical sectioning microscopy

3.1 Diffuser-based temporal focusing microscopy: generating temporal focusing without high-order diffraction

In this section I would like to present a simple approach by which we resolved the limitations associated with single excitation wavelength and low acquisition rates in the original temporal-focusing microscopes. As discussed previously, the optical path of conventional temporal-focusing microscopy is wavelength-dependent because the diffraction angle of a high-order diffracted beam depends on the central wavelength of the excitation light. One way to overcome this limitation is to use a ground-glass diffuser rather than a blazed grating as the scattering plate, or, in terms of diffraction, to use 0th-order diffracted beams rather than high-order diffracted beams. An illustration of such an optical system can be found in Fig. 3.1. The scattering pattern of a ground-glass diffuser is dominated by zero-order diffraction, and thus the optical path is insensitive to the central wavelength of the excitation light. The original report of temporal focusing by Oron et al., however, suggests that using ground-glass diffusers to create sufficient temporal-focusing effect requires the pulse durations of the laser to be shorter than 10 fs, even with high numerical-aperture (NA) objectives [6]. This would make diffuser-based temporal focusing almost impractical, given the current pulse durations of most commercially available light sources (~ 100 fs). In their estimations, though, the ground-glass

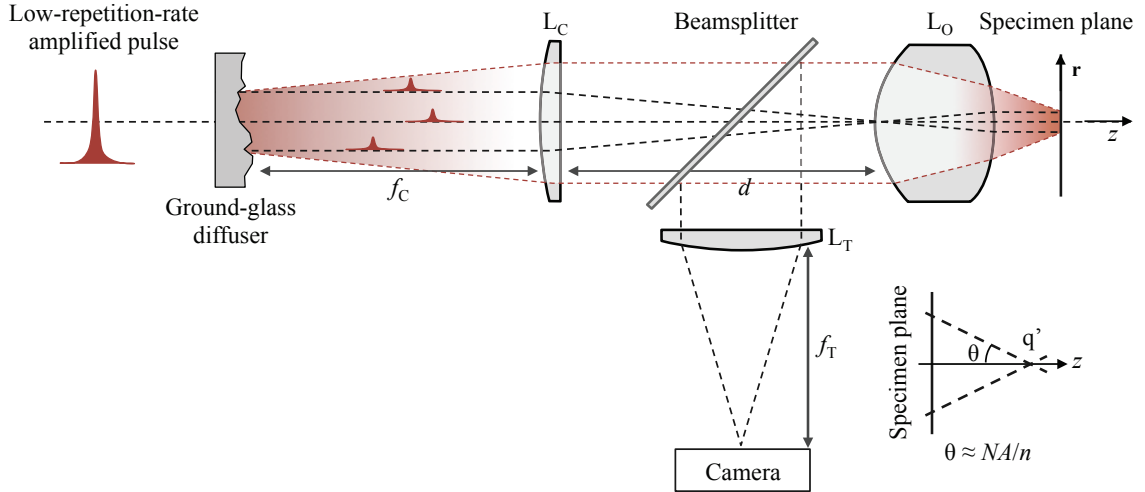


Figure 3.1: The setup of a diffuser-based temporal focusing microscope. The ultrafast infrared laser beam from the left is scattered by a ground-glass diffuser. The image of the surface of the diffuser is then projected to the sample to excite a thin plane. L_1 : microscope objective of focal length f_O . L_2 : collimation lens of focal length f_C . L_3 : tube lens of focal length f_T .

diffuser was considered as an ideally flat plane of points generating ultrafast pulses simultaneously. In fact, ground-glass diffusers have rough surfaces, wherein the height differences from one point to another can introduce random time delays among the scattering microstructures. In other words, a ground-glass diffuser can actually create a plane of point-like sources with a random distribution of time delays with respect to one another, instead of zero time delays as was previously modeled. By projecting these point sources onto the specimen plane of the microscope, temporal focusing and hence optical sectioning can be achieved. Through geometrical calculations, we found that using an ground-glass diffuser should enable optical sectioning comparable to confocal microscopy, even with objectives of moderate numerical apertures and pulse durations up to 100 fs.

The original temporal focusing microscopy demonstrated by Oron et al. in 2005 [6] has another issue: low acquisition rates. Although one of the main purposes of developing temporal focusing microscopy is to improve the imaging speeds of optical-sectioning imaging, the frame rate achieved by the original setup is around 0.03 frame per second, much slower than commercial single-point-scanning systems even at that time. Here we should note that the limiting factor of the original temporal focusing setup is not instrumentations, but the signal-to-noise ratio of the acquired images. In that setup, Oron et al. used the pulse train from an ultrafast oscillator, which is commonly

used for conventional single-point-scanning multiphoton excitation fluorescence microscopy, as the excitation light source. In Section 3.1.1 we can see how such a setup results in low signals, and how the signals can be enhanced by using amplified, low-repetition-rate pulse trains. This approach is also suggested by Oron et al. [6]. In Section 3.1.3 we demonstrate that by using a ground-glass diffuser and a laser source of a low repetition rate and high pulse energy, we can obtain volumetric fluorescence images of fluorescent protein-labelled living epithelial tissue at a frame rate of 5 frames per second (fps), similar to that used in a conventional epifluorescence microscope to obtain images on the same sample. Although the axial resolution of our method is roughly 3 times coarser than that of conventional confocal microscopy, it is more than 2 times finer than that achieved by the original grating-based temporal focusing microscopy.

3.1.1 Theoretical estimations

The efficiency of temporal focusing through an optical diffuser

In this section we estimate the temporal focusing effect created by a ground-glass diffuser. Specifically, we compute the variation of the pulse duration along the optical axis based on geometric optics.

Figure 3.1 depicts the schematic of our setup. An ground-glass diffuser was used to transform the incoming ultrafast laser beam into a plane of point sources. These point sources were then projected onto the specimen plane of an infinite-corrected microscope, through the collimation lens L_C and the objective lens L_O . The emitted fluorescence was imaged onto a camera through a tube lens L_T .

As discussed by Oron et al., the elongation of pulse duration at an out-of-focus point q' at a distance z away from the scattering plate can be approximated by the maximal difference of pulse arrival times from the point sources within a cone of angle θ from the scattering plate (Fig. 3.1 inset) [6]. Here, θ can be determined by the divergence angle of L_O , $\theta \approx NA/n$ (Fig. 3.1 inset) [6]. To estimate the difference of pulse arrival times resulting from the geometry of the setup, we first considered the case where the diffuser is approximated as a flat plane of point sources wherein

there is no time delays among one another. Using the lens formula and paraxial approximation, the elongation of pulse duration Δt_G at the point q' can be estimated as

$$\Delta t_G(z) \approx \frac{(f_C + f_O - d) \cdot \text{NA}^2}{2c \cdot n \cdot f_O^2} \cdot z^2 + n \frac{n - \sqrt{n^2 - \text{NA}^2}}{c \cdot \sqrt{n^2 - \text{NA}^2}} \cdot z \quad , \quad (3.1)$$

where c is the speed of light in vacuum and n is the refractive index of the sample medium. The first term on the right hand side arises from the length differences of different optical paths from the diffuser to specimen plane, and the second term results from the length differences of optical paths from the specimen plane to point q' .

We next take into account the surface roughness of the diffuser and estimate how such roughness leads to a randomness of arrival times. To proceed, let us consider a surface structure depicted in Fig. 3.2. In this case, an ultrafast pulse enters a ground-glass diffuser through the flat surface and exits from the rough surface where it transforms to a plane of point sources, and the time delays between pulses P_1 and P_2 can be estimated as:

$$\Delta t' = \frac{\Delta l}{c} = \frac{(h_1 + l_1) - (h_2 + l_2)}{c} = \frac{(h_1 - h_2) + (l_1 - l_2)}{c}. \quad (3.2)$$

From the geometry in Fig. 3.2 it is straightforward to derive that:

$$\frac{h_1}{c} + \frac{nl_1}{c} = \frac{h_2}{c} + \frac{nl_2}{c}, \quad (3.3)$$

and therefore:

$$h_1 - h_2 = -n(l_1 - l_2), \quad (3.4)$$

where n is the refractive index of glass (≈ 1.5). As a result, the time delay between P_1 and P_2 is $(n - 1) \cdot (h_2 - h_1)/c \approx 0.5 \Delta h/c$. Now we can generalize this estimation such that the overall time delay caused by the roughness in a certain region A_r of radius r (the conjugate region and radius on the specimen plane are denoted as A'_r and r' respectively) on the diffuser surface can be estimated

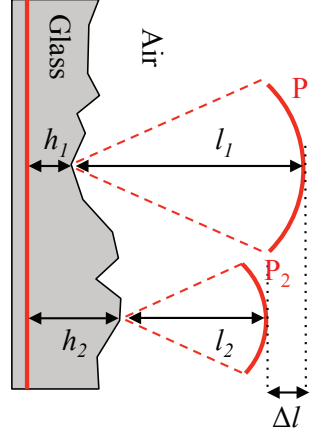


Figure 3.2: Illustration of time delays generated by the surface roughness of a ground-glass diffuser.

as:

$$\Delta t' \approx 0.5 \frac{\Delta h}{c}, \quad (3.5)$$

where Δh is the maximal surface height discrepancy within A_r .

As its name suggests, the roughness of an ground-glass diffuser is made by grinding a glass surface with particles of sizes less than a certain length D . Thus, we expect $\Delta h \rightarrow 0$ when $r \rightarrow 0$, and $\Delta h \approx D$ if $r \gg D$, as shown in Fig. 3.3. To take into account these asymptotic estimations, we used a simple approximation here: $\Delta h \approx \alpha \cdot 2r$ if $\alpha \cdot 2r < D$ and $\Delta h \approx D$ if $\alpha \cdot 2r \geq D$, where α is a dimensionless roughness parameter of a ground-glass diffuser. Using this approximation, we obtain a simple estimation of the difference of arrival times $\Delta t'$ within $A_{r'}$,

$$\Delta t' = \begin{cases} \frac{\alpha f_C}{c f_O} \cdot r' & \text{if } \frac{\alpha f_C}{f_O} \cdot r' < 0.5 D \\ \frac{0.5 D}{c} & \text{if } \frac{\alpha f_C}{f_O} \cdot r' \geq 0.5 D \end{cases} = \frac{1}{c} \cdot \text{Min} \left[\frac{\alpha f_C}{f_O} r', 0.5 D \right]. \quad (3.6)$$

For the out-of-focus point q' shown in Fig. 3.1 (inset), $A_{r'}$ corresponds to the area covered by the cone angle θ , and so we have $r' \approx z \cdot \theta \approx \frac{\text{NA}}{n} z$ and

$$\Delta t'(z) = \frac{1}{c} \cdot \text{Min} \left[\frac{\alpha f_C}{f_O} \cdot \frac{\text{NA}}{n} \cdot z, 0.5 D \right] \quad (3.7)$$

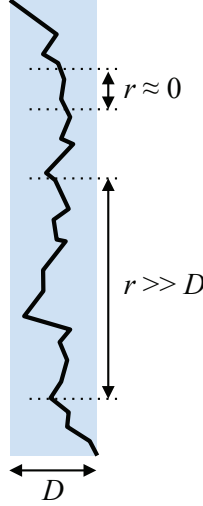


Figure 3.3: Illustration of surface roughness of a ground-glass diffuser. Let Δh denote the maximal surface height discrepancy (i.e., the peak-to-valley difference) within an area of radius r (the conjugate radius r' on the specimen plane is of radius $r f_O/f_D$), we have $\Delta h \rightarrow 0$ when $r \rightarrow 0$, and $\Delta h \approx D$ when $r \gg D$.

Combining eqs. 3.1 and 3.7, we finally obtain the effective pulse duration at an out-of-focus point q' at distance z from the specimen plane, namely

$$\begin{aligned} \tau_{\text{eff}}(z) &= \tau_0 + \Delta t' + \Delta t_G \quad (3.8) \\ &= \tau_0 + \frac{\text{Min} \left[\frac{\alpha f_C}{f_O} \frac{\text{NA}}{n} z, 0.5 D \right]}{c} + \frac{(f_C + f_O - d) \text{NA}^2}{2 c n f_O^2} z^2 + n \frac{n - \sqrt{n^2 - \text{NA}^2}}{c \sqrt{n^2 - \text{NA}^2}} z, \quad (3.9) \end{aligned}$$

where τ_0 is the pulse width of the laser source.

Figure 3.4 shows the numerical results of $\tau_{\text{eff}}(z)$ for the cases of three different objective lenses commonly used for biomedical microscopy. Consistent with the report of Oron et al. [6], we find that the contribution of Δt_G to $\tau_{\text{eff}}(z)$ is negligible when $z \approx$ Rayleigh length z_R . Nevertheless, in this small z regime, $\Delta t'$ in eq. 3.9 can lead to a significant elongation of pulse width. In particular, for the small z regions where $\frac{\alpha f_C}{f_O} \cdot \frac{\text{NA}}{n} \cdot z < 0.5 D$, eq. 3.9 can be simplified as:

$$\tau_{\text{eff}} \approx \tau_0 \left(1 + \frac{\alpha f_C}{f_O} \cdot \frac{\text{NA}}{\tau_0 n c} z \right) = \tau_0 \left(1 + \frac{\alpha f_C}{f_O} \cdot \frac{n \lambda}{\pi \tau_0 c \text{NA}} \bar{z} \right), \quad \text{with } \bar{z} \equiv \frac{z}{z_R} \approx \frac{\pi \text{NA}^2}{n^2 \lambda} z. \quad (3.10)$$

Here, \bar{z} is defined in units of Rayleigh length in order to facilitate the comparison of our results with

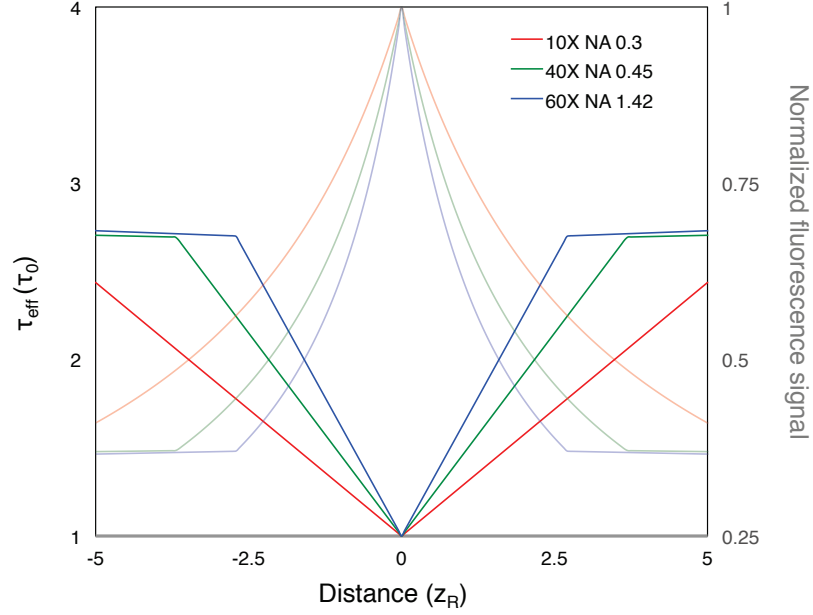


Figure 3.4: Effective pulse durations and two-photon excitation strengths as functions of z under different objective lenses. The numerical results were obtained from eq. 3.9. Notice that eq. 3.11 predicts $\bar{z}^* \approx 3.53, 2.21,$ and 1.62 for these objective lenses, respectively, which are comparable with the numerical results. The inverse of τ_{eff} was used to represent $S_{2\text{p}}$ (see eq. 3.15). The horizontal (distance) and vertical (τ_{eff}) axes are expressed in units of Rayleigh length and τ_0 , respectively. Parameters: $f_C = 180$ mm, $D = 100$ μm , $d = 200$ mm, $\lambda = 800$ nm, and $\tau_0 = 100$ fs. Objective lens 10X: NA=0.3, $f_O = 18$ mm, $n = 1$. Objective lens 40X: NA=0.75, $f_O = 4.5$ mm, $n = 1$. Objective lens 60X: NA=1.1, $f_O = 3$ mm, $n = 1.33$ (water immersion).

conventional confocal and two-photon scanning microscopy. We further define

$$\bar{z}^* \equiv \frac{f_O}{f_C} \cdot \frac{\pi \tau_0 c \text{NA}}{n \lambda} = \frac{\pi \tau_0 c}{\lambda \alpha f_C} \cdot \frac{f_O \text{NA}}{n}, \quad (3.11)$$

whereby at $\bar{z} = \bar{z}^*$, $\tau_{\text{eff}} \approx 2\tau_0$, i.e., $z = z_R \bar{z}^*$ indicates positions at which the effective pulse width is doubled. For two-photon excitation, this corresponds to the positions where the fluorescence signal drops to half of the maximum. In conventional confocal and two-photon scanning microscopy, the corresponding \bar{z}^* is ~ 1 . From the calculations outlined in Fig. 3.4, we find that optical sectioning is comparable with conventional confocal microscopy, with either moderate (0.3-0.75) or high (>1) NA objectives. Moreover, we find that laser pulses of 100-fs durations are sufficient to provide such sectioning effects.

The efficiency of multiphoton excitation at low repetition rate

To solve the limitation of low frame rate, we next examine how the repetition rates of pulsed lasers influence the efficiency of two-photon excitation (at constant average power). In short, we find that a 10^5 -fold increase in signal-to-noise ratios is obtained by lowering the repetition rate from 100 MHz to 1 kHz, thus providing a signal level comparable to that of conventional multiphoton excitation fluorescence microscopy.

For simplicity, we consider a two-photon excitation process and estimate the light intensity required for wide-field two-photon excitation. For square pulses, the fluorescence signal obtained from a single laser pulse at a single pixel can be estimated as:

$$s_{2p} = \beta \cdot I_p^2 \cdot \tau \quad , \quad (3.12)$$

where β is the two-photon excitation coefficient, I_p is the peak intensity of the excitation pulse, and τ is the pulse duration. Within a time unit, the fluorescence signal from each pixel collected at the array detector (camera), S_{2p} , depends on the repetition rate of the pulsed laser f as

$$S_{2p} = s_{2p} \cdot f. \quad (3.13)$$

On the other hand, within a time unit, the average intensity of the pulsed laser on a single pixel is

$$I_{\text{avg}} = \tau \cdot I_p \cdot f. \quad (3.14)$$

Combining eqs. 3.12, 3.13 and 3.14, we have

$$S_{2p} = \beta \cdot \frac{I_{\text{avg}}^2}{f \cdot \tau} \propto \frac{1}{f}, \quad (3.15)$$

which suggests that for a fixed average intensity I_{avg} , the signal level can be significantly enhanced by reducing the repetition rate f . For example, lowering f from 100 MHz to 1 kHz can increase the

signal 10^5 -fold without increasing the average light intensity delivered to the specimen. It should be noted that the I_p of our low-repetition-rate setup is of similar order of magnitude as that used in high-repetition-rate point-scanning microscopies. Thus, the signal levels of these two schemes are predicted to be comparable.

3.1.2 Methods and Materials

The light sources we used in this work are ultrafast chirped pulse Ti:Sapphire amplifiers. Two different models were used for the convenience of collaborations. Live-cell imaging was studied (see Fig. 3.6) with a Spectra-Physics[®] Spitfire[®] Pro, seeded with a Spectra-Physics[®] Mai Tai[®] SP ultrafast oscillator situated parallel to the amplifier within an enclosure. Measurement of axial responses was carried out with a Coherent[®] Legend Elite-USP-1k-HE, seeded with a Coherent[®] Mantis-5 ultrafast oscillator located parallel to the amplifier. The pulse durations, defined as the FWHM of the temporal profiles of both amplifiers was approximately 35 fs or less. The wavelength of both amplifiers was centered approximately at 800 nm with FWHM ≈ 30 nm. We expanded the beam size by telescoping such that the beam profile on the diffuser was 2D Gaussian with FWHM ≈ 20 mm. The maximal output of the laser amplifier was ~ 3 Watt (average power), and was attenuated to avoid thermal damage to biological specimens. The average laser powers reported in the following sections were all measured at the back aperture of the objective lens L_O .

The ground-glass diffuser employed was a Thor Labs model DG10-120. Diffusers, in general, can cause significant inhomogeneities of the light intensity at the image plane. To reduce these inhomogeneities, glass etching cream (Armour Etch[®]) was used to etch the diffuser. The roughness parameters D and α of the diffuser were found to be $30 \mu\text{m}$ and 0.1 after etching, according to the surface profile we measured.

As shown in Fig. 3.1, the collimated laser beam is scattered by the ground-glass diffuser, collimated by the diffuser lens L_C , and then projected to specimen plane via the objective lenses (LUMFLN 60XW NA 1.1, PLANAPO N 60X NA 1.42). The LUMFLN model objective was used for the living biological samples owing to its long working distance. The PLANAPO objective was

used for the quantitative characterizations and the fixed biological sample.

The chromatic dispersion of the full optical path was pre-compensated by the built-in compressor of the ultrafast amplifiers such that the signal level at the specimen plane was maximized. Images were obtained by a CCD camera (iXon DU-885K, Andor) through L_T . The field of view is a ~ 6.4 -by- $6.4 \text{ mm}^2/M_O$ square, where M_O is the nominal magnification of L_O . The illumination field is 2D Gaussian with FWHM $\approx 20 \text{ mm}/M_O$. A larger illumination field or more uniform profile can be obtained by further expanding the laser beam before the ground-glass diffuser.

The axial resolution was determined by taking images along the optical axis of a thin layer (thickness less than $2 \mu\text{m}$) of fluorescein (F-1300, Invitrogen). For living-cell imaging, we used human mammary gland MCF-10A cells expressing cyan fluorescent protein-conjugated histone (H2B-cerulean), which binds to chromosomes and has been widely used to indicate cell nuclei. MCF-10A cells were seeded in 3-D matrigel (BD MatrigelTM) for 10 days to form bowl-shape cell clusters of several hundred micrometers in size. We then used the cell clusters to evaluate the high-frame-rate acquisition and optical sectioning capabilities of our diffuser-based temporal focusing microscope. Following the acquisition of optical sections, three-dimensional views of the epithelial tissue were reconstructed using 3-D Viewer of ImageJ.

3.1.3 Results

The axial resolution of diffuser-based temporal focusing microscopy is comparable to conventional confocal microscopy

Figure 3.5 shows the axial resolution of the optical setup depicted in Fig. 3.1. Axial resolution was determined by the FWHM of measured axial response. With $M_O = 60$, $\text{NA} \approx 1.42$, $n \approx 1.5$, the axial resolution was found to be $\sim 2 \mu\text{m}$, and the corresponding $\bar{z}^* \approx 3$. This is comparable to the axial resolution of an optimized conventional confocal microscope, which has $\bar{z}^* \approx 1$. Note that it should be possible to obtain an axial resolution of $\bar{z}^* \approx 1$ by optimizing the microscope design, as we discuss in Section 3.1.4.

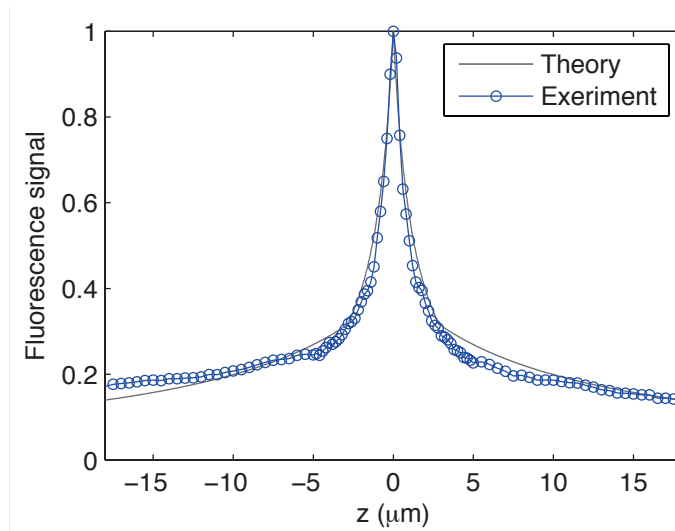


Figure 3.5: Theoretical (grey line) and measured (blue circles) axial response of our diffuser-based temporal focusing microscopy. The fluorescence profile was obtained by taking optical sections of a homogeneous dye film (thickness less than $2\ \mu\text{m}$). The signal was determined by the integrating the intensity of each section. The profile was normalized by its maximum. The FWHM here is $\sim 2\ \mu\text{m}$, while the theoretical axial resolution of a confocal microscope with the same objective is $\sim 0.8\ \mu\text{m}$ [27, 28]. Parameters in theoretical estimation and experiment: $M_O = 60$, $\text{NA} = 1.42$, $n = 1.5$ (oil immersion), $f_O = 3\ \text{mm}$, $f_C = 180\ \text{mm}$, $\tau_0 = 35\ \text{fs}$, $d = 200\ \text{mm}$, $\lambda = 800\ \text{nm}$, $\alpha = 0.1$, $D = 30\ \mu\text{m}$.

The frame rate of diffuser-based temporal focusing microscopy is comparable to conventional epifluorescence microscopy for living-cell imaging

To demonstrate that diffuser-based temporal focusing microscopy has the capability of imaging living cells and tissues at high frame rates, we performed optical sectioning of living, three-dimensional MCF-10A cell clusters of hemispherical shapes (3.6). Here, the exposure time was set at 200 ms, equivalent to 5 fps, which is around 10 times faster than the conventional single-point-scanning multiphoton excitation fluorescence microscope we also used to image the same specimen, and is 150 times faster than a temporal focusing setup using a non-amplified 75-MHz Ti:Sapphire oscillator to image cells stained with (much brighter) fluorescent dye [6]. Such an exposure time lies within similar orders of magnitude of that typically used in conventional epifluorescence microscopy (~ 10 -100 ms), which we also used to image the same specimen (Epi in Fig. 3.6) illuminated by a mercury vapor lamp (X-Cite[®] 120Q, Lumen Dynamics, attenuated by OD 2 to prevent photobleaching). Orthogonal views in Fig. 3.6 also demonstrates resolution of the boundaries of cell nuclei along the z axis. Images obtained by diffuser-based temporal focusing microscopy (D-TFM) show spots in oval

shapes, resembling the normal shape of cell nuclei. In contrast, the orthogonal view obtained by epifluorescence microscopy shows distortion of the proper cell nuclear shape, due to the spreading of the out-of-focus signal in an epifluorescence microscope. These results suggest that diffuser-based temporal focusing microscopy can achieve high-frame-rate optical sectioning on living cells.

Inhomogeneity of the illumination field can be reduced by rotating the diffuser

In this study, we found that conventional diffusers can cause a significant inhomogeneity of the light intensity in the illumination field, i.e., bright spots. The observed field inhomogeneity leads to inhomogeneous sectioning capability across the field of view, the level of which can be measured by imaging a homogenous dye film, then separating the field of view into several areas and comparing the FWHMs of their axial responses. In our setup, the standard deviation of the FWHMs was found to be $\sim 0.3\mu\text{m}$. One way to reduce this inhomogeneity is through the use of multiple diffusers. However, each diffuser would generate a certain level of time delay and thus contribute to pulse broadening. As an alternative solution, we have chosen to simply rotate the diffuser. By rotating the optical diffuser during the acquisition of a single frame, the inhomogeneities in the illumination field are averaged out. This effect is demonstrated in Fig. 3.7.

3.1.4 Discussion

Optimization and limit of axial resolution

Equation 3.11 suggests that \bar{z}^* can be further reduced by using an objective with a higher magnification and NA (which often exhibits a smaller $\frac{f_O \text{NA}}{n}$), as shown in Fig. 3.4. Likewise, increasing f_C , α , or reducing τ_0 leads to smaller \bar{z}^* . We should note that these estimations are derived based on geometrical optics, and are not valid when $\bar{z}^* < 1$, in which case the optimal axial resolution of our temporal focusing setup would be the same as that of a single-point-scanning multiphoton excitation fluorescence microscope [6].

A fundamental advantage of diffuser-based temporal focusing over grating-based approaches is that the diffuser-based technique can achieve the axial resolution of a single-point-scanning setup,

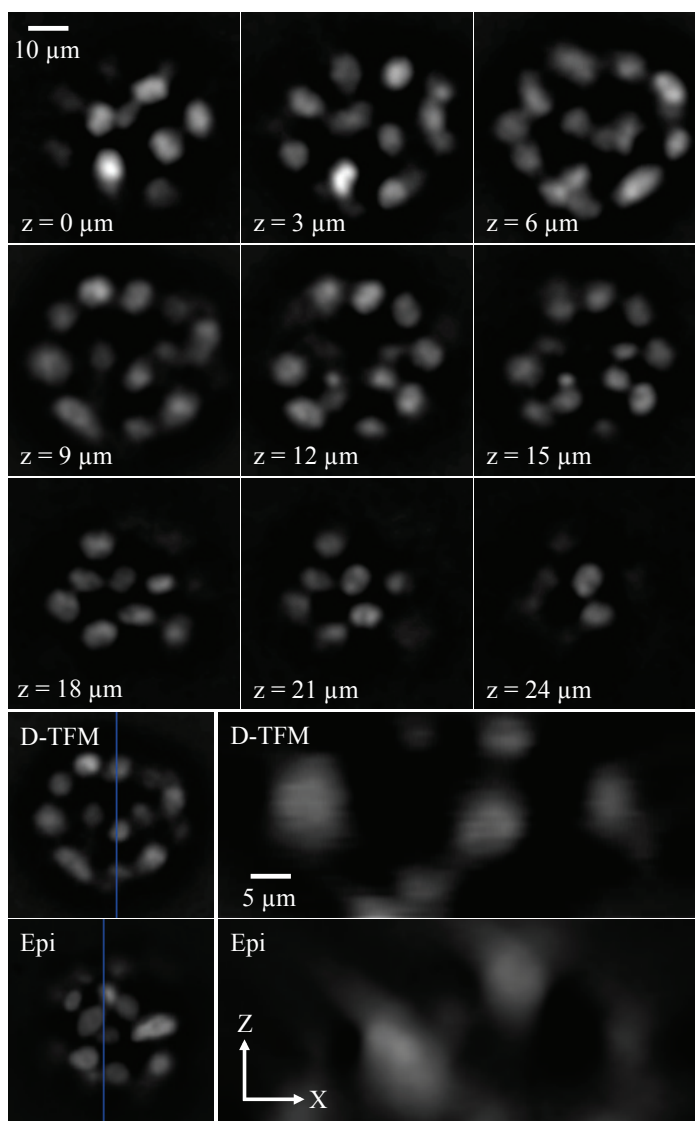


Figure 3.6: Optical sections and orthogonal views of living MCF-10A cells in a hemispherical structure. The top panel shows the images obtained at sequential depths. The bottom panels show the reconstructed orthogonal views under a diffuser-based temporal focusing microscope (D-TFM) and a conventional epifluorescence microscope (Epi), respectively. In the orthogonal view from the epifluorescence microscope, we clearly observe the residual out-of-focus light at the top and bottom edges of the nuclei. The blue lines indicate the positions where the orthogonal views were taken. Fluorescence signals were from cell nuclei expressing cyan fluorescent protein-conjugated histone (H2B-cerulean). Exposure time of each frame: 0.2 seconds. L_O : 60X, $NA \approx 1.1$, $n \approx 1.33$. Step size: 1 μm . Laser average power: <10 mW.

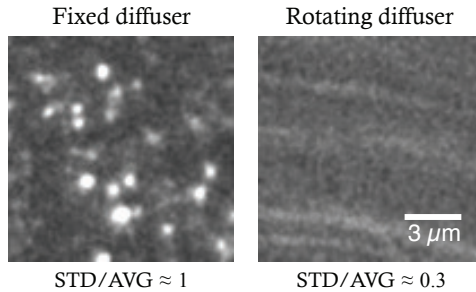


Figure 3.7: Illumination field intensity inhomogeneity with fixed (left) and rotated (right) optical diffusers. The field inhomogeneity is defined as the standard deviation (STD) of the field divided by the average (AVG) intensity of the field. The field inhomogeneity is greatly reduced by rotating the optical diffuser during the exposure of each frame. The sample is a homogeneous dye layer.

whereas (single) grating-based temporal focusing is limited to that of a line-scan setup. The difference arises from the way in which the time delays are generated. For ground-glass diffusers, the time delay results from the surface roughness of the diffusers, which creates a two-dimensional spatial profile for the randomness of the time delay. In contrast, the time delay in grating-based temporal focusing is created by the one-dimensional scan of the laser pulses on the grating surface. This restriction has been overcome by using two orthogonally aligned gratings [29]. In such a setup, the two gratings must differ in groove density sufficiently, such that the scanning of the laser pulse can be well separated in two orthogonal dimensions [29]. Such a design increases the complexity of the apparatus and will likely require multiple pairs of gratings when multiple/tunable excitation wavelengths are used.

From eq. 3.7, the spread, or distribution, of arrival times produced from the surface roughness of a diffuser is upper bounded by the factor D . This suggests that diffusers with larger D should be used to ensure a sufficiently large spread of arrival times. The roughness of the diffuser surface, however, leads in turn to roughness of the image plane, D' . Using the thin lens formula, we estimate D' to be $(\frac{f_O}{f_C})^2 D$. This suggests that D' can be negligible if $f_C \gg f_O$. Thus, with a proper arrangement of parameters, the roughness of the image plane can be reduced below one Rayleigh length, while the surface roughness of the diffuser is sufficiently large to create temporal focusing.

Limitation of frame rate and benefits of low repetition rate

For living-tissue imaging, the frame rates of our setup are limited by the relatively low excitation efficiency (compared with organic fluorescent dyes) of fluorescent proteins expressed in living systems. Nevertheless, eq. 3.15 suggests that signal-to-noise ratios can be further enhanced by lowering the repetition rate while maintaining the average power of the laser. For example, the frame rate of our setup can be further increased by equipping our system with a pulsed laser of much lower repetition rate, e.g., 100 Hz. With such a low repetition rate, eq. 3.15 suggests a 10-fold stronger signal-to-noise ratio than what is presented in this study. This would lead to a frame rate of up to 50 fps, a rate sufficient to study most biological processes such as cell division, migration, and polarity formation. Here we estimate the limit of frame rates based on imaging the fluorescent proteins expressed in living systems. This limitation is relaxed, though, if the signals are derived from materials with strong fluorescence efficiency such as fluorescent dyes and nanoparticles.

Our setup can achieve the large field of view with a relatively short exposure duration simply because the 1-kHz amplifier is very powerful; that is, because it is supplying its average power at a low repetition rate and low duty cycle and thus achieving a high peak power. To generate multiphoton excitation at the level required for imaging with reasonable frame rates, the peak intensity is commonly around or greater than $1 \text{ kW}/\mu\text{m}^2$ [2]. Therefore, to excite an area up to 1 mm^2 , one needs a light source with peak power greater than 10^9 Watt. The maximal peak power of our amplifier is roughly 10^{11} Watt, and is thus powerful enough to support a large field of view for most microscopy applications. It should be noted that in the original temporal focusing setup [6], a 140-by-140- μm field of view was obtained with an average power of 30 mW and an exposure time of 30 seconds. This indicates that a 1-mm^2 field of view can be achieved with that instrument by using a low magnification objective and an average power of around 1.5 Watt, though the exposure time in such a setup could be slightly longer than 30 seconds because lower magnification objectives are typically less efficient in collecting light.

However, from a biologist's point of view, we would also like to point out that discussing the imaging speed for fixed biological samples stained with fluorescent dye is less important than the

speed achievable for living systems. Once a sample is fixed, using an imaging time of either 3 hours or 10 seconds would most likely provide the same level of details and information. On the other hand, for the studies of dynamic biological process, the imaging speed would determine the temporal resolution of the observations. To the best of our knowledge, this is the first report of imaging live cells expressing fluorescent protein by a temporal focusing microscope at a frame rate faster than 1 fps.

In addition to the enhancement of the signal level and frame rate, there are certain potential benefits provided by lowering the repetition rate from the MHz to kHz regime. It has been reported that the use of low repetition rates (at the same optical power) can reduce photobleaching [30, 31]. This is achieved through the avoidance excitation during dark state conversion, which is believed to be a photobleaching mechanism. Indeed, a 5- to 25-fold enhancement of total fluorescence yield, before detrimental effects from photobleaching, has been experimentally measured [30]. Moreover, lowering the repetition rate is equivalent to providing the system a longer window of no excitation. This would allow slow processes such as heat dissipation to occur more efficiently, thus minimizing sample damage caused by a continuous accumulation of heat. As a result, even with a similar amount of thermal energy introduced by the excitation process, a sample excited at a low-repetition-rate light pulses is less likely to be damaged by heat accumulation as compared to the use of a high-repetition-rate light pulses [17].

Potential applications as structured illumination microscopy

In principle, the inhomogeneity of the illumination field can be utilized for structured illumination microscopy [3]. This could be particularly useful in applications where reasonable optical sectioning, as provided by temporal focusing, is not achievable. Examples include coherent anti-Stokes Raman scattering (CARS) and stimulated Raman scattering microscopy, where picosecond pulses are generally required to obtain chemical specificity [32, 33]. Based on Equation 3.11, ultrafast pulse trains of picosecond duration would greatly reduce the sectioning effect. Nevertheless, by using the inhomogeneity of the illumination field as a structured light source, it is possible to regain sectioning

capability of these systems, as demonstrated in a previous study [3]. This allows one to integrate CARS with multiphoton excitation in a wide-field microscope simply by using a ground-glass diffuser.

3.1.5 Brief summary

The question of how to increase image acquisition rate and axial resolution, while maintaining a bio-compatible laser dosage, is a long-standing challenge in the community of optical microscopy. In this report, we have demonstrated a microscope design for living-tissue imaging that provides an axial resolution comparable to confocal microscopy and a frame rate similar to that of epifluorescence microscopy.

By utilizing an ground-glass diffuser, a temporal focusing setup is realized with a design as simple as a conventional epifluorescence microscope. Even at a high frame rate, the photobleaching and thermal damage of diffuser-based temporal focusing microscopy could be lower than single-point-scanning multiphoton excitation fluorescence and confocal fluorescence microscopy. Compared with temporal focusing techniques using MHz repetition-rate laser pulse trains, the use of low repetition-rate pulses, while maintaining the same average power, can significantly enhance the signal-to-noise ratio. In addition, using an ground-glass diffuser instead of a blazed diffraction grating provides flexibility for multi- or tunable-wavelength light sources, and thus creates a platform for multi-spectral imaging and pump-probe microscopy. Taken together, these features suggest that diffuser-based temporal focusing microscopy can be used to study fast, three-dimensional processes in living cells and tissues, and to do so with minimal photo-toxicity and thermal damage.

3.2 Temporal focusing or dense time multiplexing by height-staggered microlens array

In previous sections we see how time delays and temporal focusing can be generated using 0th-order diffracted beams rather than high-order diffracted ones so as to avoid wavelength dependent optical paths. However, we see that the usage of ground-glass diffusers also introduce inhomogeneity of

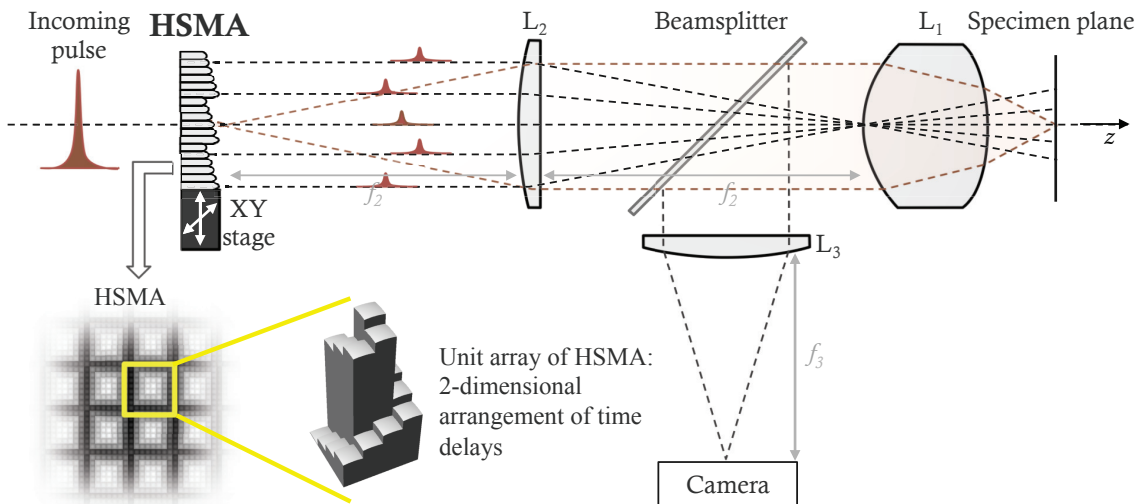


Figure 3.8: Setup of a HSMA-based temporal focusing microscope. L_1 is the microscope objective lens. L_2 and L_3 are tube lenses of focal length f_T . XY stage performs the lateral translations of the multifocal pattern. The specimen plane is defined as the focal plane of the objective lens L_1 . Insets illustrate a spiral HSMA used in this study.

illumination field. Although shifting or rotating the diffuser during exposure can mitigate such inhomogeneity, it can also decrease frame rates greatly. Other issues of diffuser-based temporal focusing include moderate axial resolution and inefficient uses of the excitation light. All of these drawbacks, interestingly, trace back to the random scattering structures of ground-glass diffusers.

To further improve the field homogeneity and axial resolution and to use excitation light efficiently, we proposed to use a new optical element that has engineered scattering structures for generating temporal focusing: an array of microlenses with height differences among one another. Figure 3.8 shows the schematic of such a microscope. This height-staggered microlens array (HSMA) has a constant lens pitch across the entire array, so that field homogeneity can be achieved by simply shifting the array for a few steps. The focusing power of individual microlenses can be made to match the back aperture of the objective lens so that each focus shows axial response similar to that of a single-point-scanning multiphoton excitation fluorescence microscope near the focal plane of the objective lens. At out-of-focus regions, the height staggering among the microlenses can introduce time delays which leads to temporal focusing effect and thus reduces out-of-focus excitation.

In this section, we discuss how to implement such a concept and how to estimate its optical

performance; we also experimentally compare its axial response with that of a confocal microscope, and demonstrate sectioning imaging on living *C. elegans*. We should note here that the combination of microlens arrays and temporal masks, as used in time-multiplexed multifocal multiphoton microscopy (TM-MMM) [5], can provide equivalent functions of the proposed HSMA, although additional precision alignment and positioning are required.

Before diving into the details of our HSMA-based temporal focusing technique, it is worthwhile to discuss the difference between our technique and TM-MMM. While both of these techniques reduce out-of-focus excitation by introducing time delays among foci, the goals of system optimization are different. In TM-MMM, an upper limit of out-of-focus excitation is set and the goal of optimization is to arrange foci as (spatially) close to one another as possible until this limit is reached [5]. Because in the original TM-MMM this limit is set almost as low as that in single-point-scanning multiphoton microscopy, the result of such optimization, as we can see later, is that the foci are far apart from one another and thus a large number of scanning steps (~ 100 or larger) are required to illuminate the entire field of view. Our approach, on the other hand, fixes the interfocal distances at around twice of the diameter of a focal spot so that only $\sim 4-10$ scanning steps are required to fulfill the field of view, and we try to minimize out-of-focus excitation by manipulating the distribution of time delays among foci. The disadvantage of such an approach is that the out-of-focus excitation is moderately suppressed, and to overcome this issue we utilized the multifocal pattern to implement structured illumination microscopy [3] to remove out-of-focus signals from the acquired images.

3.2.1 Design of a HSMA-based temporal focusing microscope

We begin the design of HSMA with the consideration of their physical limitations. The dimensions of HSMA are limited by fabrication technologies as well as diffractive losses. Existing techniques cannot straightforwardly engineer micro-optics of depth variation >1 mm [34]. In addition, when we consider the HSMA as an array of time-delay channels, a light pulse propagating in one channel can leak into its neighboring channels due to the nature of diffraction. To quantify such an effect, we use a simple model consisting of two adjacent microlenses with height staggering Δh , as shown

in Fig. 3.9. When the light of wavelength λ_0 exits from channel 1 (Ch1) and propagates to distance z , diffraction theory predicts the beam size, d_B , as a function of λ_0 and z . With this regard, we consider the inter-channel leakage to be non-negligible if d_B before propagating to $z = \Delta h$ is larger than the pitch of the microlens array, d . In other words, the inter-channel leakage is negligible if

$$d_B \leq d \text{ for } z \leq \Delta h. \quad (3.16)$$

A reasonable design, as shown in Fig. 3.9, is to set the focus of Ch1 at $z = \Delta h$, so that d_B decreases upon exiting Ch1 and reaches its minimum, d_f , at $z = \Delta h$. Based on the diffraction-limited spot size of an ideal thin lens, we can estimate d_f as

$$d_f \approx 1.22 \lambda_0 \times f_{\#}, \quad (3.17)$$

where $f_{\#}$ is defined as f/d [35]. Combining eqs. (3.16), (3.17) and the geometry, we have

$$d \geq 1.22 \lambda_0 \times \frac{f}{d} \approx \lambda_0 \times \frac{\Delta h}{d}, \quad (3.18)$$

and the criterion of negligible inter-channel light leakage is thus

$$d \geq \sqrt{\lambda_0 \Delta h}. \quad (3.19)$$

To ensure the inter-channel light leakage is negligible regardless of the geometrical arrangements of distinct time-delay steps, we can substitute the largest height difference in the HSMA, Δh_{\max} , for Δh in eq. (3.19), and thus derive

$$d \geq \sqrt{\lambda_0 \Delta h_{\max}}. \quad (3.20)$$

The argument here also applies to the design of the combination of temporal masks and microlens arrays used in TM-MMM [5]. In such a case, the ends of the time-delay channels are flat surfaces, and one can use the single-slit diffraction to approximate the beam size with propagation. Such an

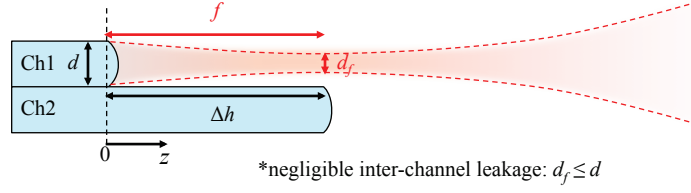


Figure 3.9: A model of two adjacent microlenses. d : aperture of the microlenses. f : focal length of the microlens. d_f : the diameter of the focal spot. Δh : height difference between two microlenses.

approach yields a similar criterion.

Accordingly, we restrict Δh_{\max} to $\sim 300 \mu\text{m}$ and $36 \mu\text{m} \geq d \geq 18 \mu\text{m}$, via eq. (3.20). These dimensions make the HSMA fabrication feasible through existing techniques, and can provide up to $\sim 10^6$ foci within a 2-inch aperture. For a simple analysis, we assume that the total amount of time delay Δt_{tot} is separated equally into N_t distinct time-delay steps (with step size Δt , eq. (3.21)). These time-delay steps are then arranged in a prescribed periodic pattern in the HSMA (Fig. 3.8 insets). Considering the propagation speed of light in a material as in the case of Fig. 3.2, we have:

$$\Delta t_{\text{tot}} \equiv (N_t - 1) \times \Delta t = \frac{\Delta h_{\max} (n - 1)}{c}, \quad (3.21)$$

where c and n are the speed of light in vacuum and the refractive index of the material of the HSMA (set to be 1.5), respectively.

Because of the limitation of Δh_{\max} , the estimated Δt in eq. (3.21) can be around or shorter than the pulse duration of conventional ultrafast oscillators or amplifiers above certain values of N_t . In such cases, we should take into account the temporal interferences among light pulses of different time delays. Notably, temporal masks with much larger Δt_{tot} have been proposed to avoid temporal interferences and to achieve scanningless TM-MMM [5], and here we can estimate the size of such HSMA using the criterion derived previously.

As estimated in Section 2.2.1, the number of distinct time-delay steps N_t required to achieve is ~ 280 . The appropriate values of Δt for negligible temporal interferences, as suggested in the previous study of TM-MMM [5], are equal to or larger than twice the pulse duration of the light pulse, τ_0 , i.e., $\Delta t \geq 2 \tau_0$ (where τ_0 was set as ≈ 100 fs for conventional ultrafast oscillators) [5].

Accordingly, we find that $\Delta h_{\max} \approx 33$ mm and $d \approx 0.15$ mm using eqs. (3.20)-(3.21), wherein λ and n are assumed to be ~ 800 nm and 1.5, respectively; such a Δh_{\max} falls far beyond the limits of existing fabrication techniques. Further, if one needs 1000-by-1000 foci in the field of view (FOV), the typical aperture of the entire HSMA will be as large as $1000 \times d \approx 150$ mm, which is considerably larger than the optical elements of a standard biomedical microscope.

To have fabrication-feasible HSMAs, we turn to optimizing the parameters of HSMAs. In the following sections, we construct a model that considers the temporal interferences among pulses separated by small amounts of time, and through this model we investigate how axial responses depend on the choice of N_t (and Δt) for a given Δt_{tot} , and the spatial arrangement of time delays in the HSMA.

3.2.2 Construct a physical optics-based model taking into account temporal interferences

Given the temporal focusing effect in the proposed technique, and with the non-negligible temporal interferences among the light pulses, a time-independent model such as that previously used for TM-MMM [5] is no longer sufficient for analyzing the performances of our setup. Thus, we develop a new model taking into account the time-dependent optical phase of multiple spectral components in an ultrafast pulse. For simplicity, we use a Gaussian-pulse approach, i.e., in the excited area, the electric field $E(\mathbf{r}, z, t)$ at position (\mathbf{r}, z) ($z = 0$ at the specimen plane) and time t is approximated as the Gaussian-weighted sum of a series of constant-interval (in k -space), in-phase light waves,

$$E(\mathbf{r}, z, t) = \sum_j e^{\frac{-(k_j - k_0)^2}{2\sigma_k^2}} E_{k_j}(\mathbf{r}, z) e^{-i\omega_j t}, \quad (3.22)$$

where k_0 is the central wavenumber of the pulse spectrum, and E_{k_j} is the scalar field of the light wave of wavenumber k_j . To approximate the ultrafast pulse train generated by the amplified laser system we used in experiments [36], we set $k_0 \approx 7.85 \times 10^4$ cm⁻¹ and a pulse duration τ_0 of ≈ 30 fs (by using an appropriate σ_k). We then employ the amplitude point spread function (PSF) derived

previously for high NA lenses [5, 19], E_{k_j} , as

$$E_{k_j}(\mathbf{r}, z) \approx k_j \int_0^\alpha \sqrt{\cos\theta} \sin\theta J_0(k_j r \sin\theta) e^{ik_j z \cos\theta} d\theta, \quad (3.23)$$

where α is the maximal focusing angle θ of the objective lens, and J_0 is the 0th-order Bessel function of the first kind. The objective lens used in all the simulations presented here is a 60X oil-immersion lens of NA 1.42.

Through eqs. (3.22) and (3.23) we can numerically evaluate the time-dependent amplitude PSF of an ultrafast pulse focused by a well-corrected objective lens, $E_{\text{PSF}}(\mathbf{r}, z, t)$. Having solved E_{PSF} numerically, we estimate the electric field near the specimen plane, $E_{\text{SP}}(\mathbf{r}, z, t)$, as the linear superposition of the E_{PSF} from the individual microlenses,

$$E_{\text{SP}}(\mathbf{r}, z, t) = \sum_{\mathbf{m}} E_{\text{PSF}}(\mathbf{r} - \mathbf{r}_{\mathbf{m}}, z, t - \Delta t_{\mathbf{m}}), \quad (3.24)$$

where $\mathbf{r}_{\mathbf{m}}$ and $\Delta t_{\mathbf{m}}$ are the central position and time delay of the ultrafast pulse going through the \mathbf{m} -th HSMA microlens, respectively. Through eq. (3.24), the excitation intensity profiles $I_{\text{SP}}(\mathbf{r}, z)$ can be derived by integrating the excitation intensity over time, as

$$I_{\text{SP}}(\mathbf{r}, z) = \int |E_{\text{SP}}(\mathbf{r}, z, t)|^{2n_p} dt, \quad (3.25)$$

where n_p is the number of photons required in single excitation event (here $n_p = 2$). Noteworthy, to fulfill the wide-field illumination condition and to simplify the simulations, our model assumes that a 'unit' microlens array is infinitely replicated in the transverse coordinates, as shown in Fig. 3.8. Under such a periodic condition, the physical optics properties in the projected region of one unit microlens array is sufficient to represent the entire system, and thus simplify the simulation process.

Because the system is assumed to be laterally periodic under such an assumption (referred to as the inf-HSMA model herein), the physical properties (ex. the distribution of electric field) of one unit region can be used to describe the entire system. Although the infinite replication of unit HSMA

is not realistic for either of experiments or numerical simulations, the inf-HSMA model is made tractable by assuming that, for the multiphoton excitation intensity I_{SP} at arbitrary positions, the contributions from very distant foci are negligible. In other words, one can approximate the results of using the infinitely replicated unit HSMA by considering only the contributions from the foci within a certain range. To justify such an approach, we need to examine if the computed I_{SP} becomes stationary (i.e., converging to a certain value) as the range of foci considered to contribute, defined by r_{tot} (Fig. 3.10(a)), is expanded.

To proceed, we compute time-integrated intensity I using eq. (3.25) with only the contributions to E_{SP} from the foci within a distance r_{tot} considered (Fig. 3.10(a)). Here we use I_{end} , the intensity at a given position as derived with a relatively large r_{tot} ($\approx 375 \lambda_0$, here λ_0 is the central wavelength of the light pulse), as a reference value, and plot I/I_{end} as r_{tot} increases from 0 to $125 \lambda_0$. Figure 3.10(b) shows that the values of I at all of the 100 randomly chosen positions converge to their corresponding I_{end} as r_{tot} increases. In particular, we note that when $r_{\text{tot}} \geq 62.5 \lambda_0$ (equivalent to $50 \mu\text{m}$ in physical dimensions), the error of I , defined as $|I - I_{\text{end}}|/I_{\text{end}}$, is less than 0.1%. Such results suggest that, for a given error tolerance in numerical simulations, we can use the inf-HSMA model by considering only the contributions of foci within a certain distance r_{inf} . Here, we have $r_{\text{inf}} \approx 50 \mu\text{m}$ for a 0.1% error tolerance. In the physical microscopy system, we can also use r_{inf} to determine the region wherein the inf-HSMA assumption is valid, as shown in Fig. 3.10(c). For conventional biomedical microscopes using $M = 60\text{X}$ objective lenses, the diameter of the full FOV is typically larger than $300 \mu\text{m}$. Thus, the inf-HSMA model is valid in the central region of diameter larger than $200 \mu\text{m}$. At the image plane, this region corresponds to a disk of diameter $\sim 12 \text{ mm}$ ($200 \mu\text{m} \times M$) or larger, which is able to cover most conventional cameras.

3.2.3 Optimize optical sectioning through tuning N_t and δt

To quantify the optical sectioning created by a particular design of HSMA, we calculate the axial response $S(z)$, i.e., total fluorescence signal at a depth z , through integration of $I_{\text{SP}}(\mathbf{r}, z)$ in eq. (3.25)

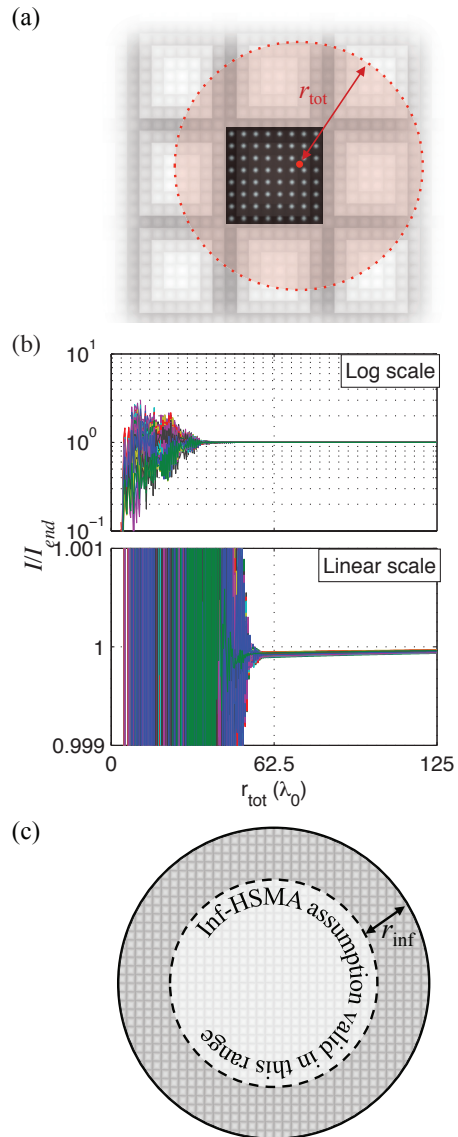


Figure 3.10: (a) The time-integrated intensity I at a particular position is numerically obtained by taking into account the contributions of foci within distance r_{tot} . The dark area with an array of bright spots indicates the calculated intensity distribution. The faded grid patterns shows the locations of microlenses when projected to the specimen plane of the microscope. (b) The convergence of I for 100 randomly picked positions (upper panel: log scale; lower panel: linear scale). Each curve represents I/I_{end} as a function of r_{tot} (see text) at a particular position. The analysis has been repeated 10 times; all results show similar convergence. (c) The area for the inf-HSMA model is valid can be determined by r_{inf} and the size of the whole FOV of the microscope.

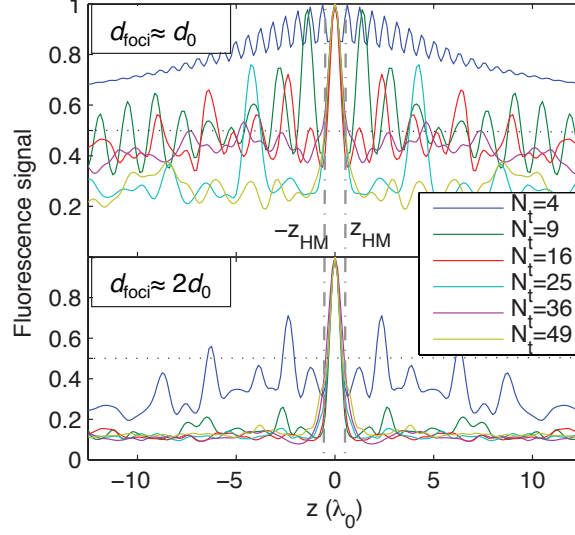


Figure 3.11: Axial responses $S(z)$ of various $(N_t, \Delta t)$ sets

over the transverse coordinates, as

$$S(z) = \int I_{\text{SP}}(\mathbf{r}, z) d^2\mathbf{r}. \quad (3.26)$$

Experimentally, $S(z)$ corresponds to the detected fluorescence signal from a thin fluorescent layer placed at a depth z .

To determine the choice of $(N_t, \Delta t)$ that produces the most efficient optical sectioning, we evaluate $S(z)$ and the ratio of out-of-focus and in-focus signal, $S_{\text{out}}/S_{\text{in}}$ (see Fig. 3.12 for illustration), for various sets of N_t and Δt (constrained by eq. (3.21)) with two interfocal spacings, $d_{\text{foci}} (\equiv d/M$, where M is the magnification of the microscopy system) $\approx d_0$ and $2d_0$.

Because of the square geometry of our HSMAs, we examine $N_t = 2^2, 3^2, 4^2, \dots$ and 9^2 . Analyzing $S_{\text{out}}/S_{\text{in}}$ reveals that the decay of the out-of-focus excitation significantly slows down between $N_t = 16$ and 64 , corresponding to $\Delta t \approx 30$ - 8 fs (i.e., $\tau_0 - 1/4 \tau_0$), for various arrangement of the distinct time-delay steps (Fig. 3.13). These results suggest that the optical sectioning for a fixed Δt_{tot} is optimized when Δt is slightly smaller than τ_0 . Further reducing Δt (equivalent to increasing N_t (eq. (3.21))) can complicate the fabrication of the HSMAs without major improvement of optical sectioning. In addition, increasing d_{foci} leads to weaker out-of-focus excitation and a less complex

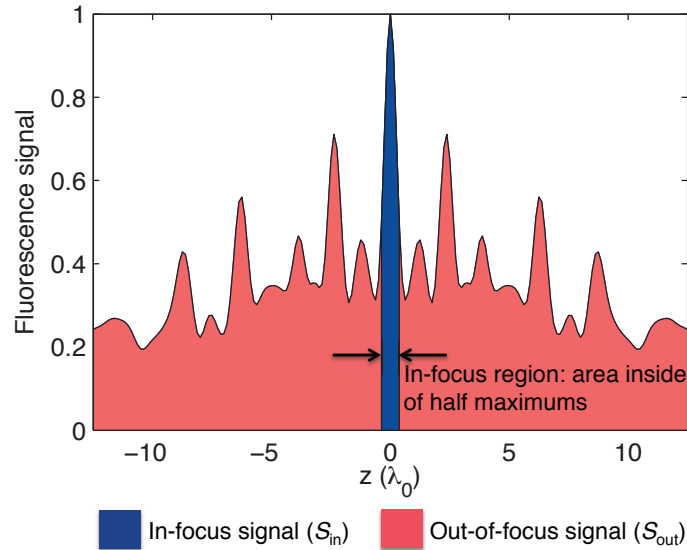


Figure 3.12: Illustration of in-focus signal and out-of-focus signal.

axial excitation profile $S(z)$ (Fig. 3.11).

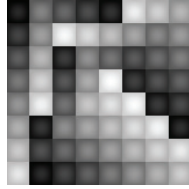
3.2.4 Experimental verification of reduction of out-of-focus excitation by HSMA

To verify the predicted out-of-focus excitation reduction in HSMA-based temporal focusing, we fabricated a height-staggered plate and experimentally conducted the axial response measurement (Fig. 3.14) by imaging a thin layer of fluorescent dye with the microscope objective translated through 200 sequential depths at $0.1\text{-}\mu\text{m}$ intervals. We made this plate using a multi-exposure protocol of photolithography (Fig. 3.15). In this protocol, the first layer of photoresist is spin-coated on the base plate and then exposed to UV light under a photo-mask, followed by soft baking of the exposed photoresist. Such a procedure is repeatedly conducted for $N_t - 1$ times to build up an N_t -level height-staggered plate. To guarantee the flatness of the surface, the photoresist is softly baked but not developed after intermediate exposures. Development was performed only after all the spin-coatings, exposures and soft-bakings were accomplished.

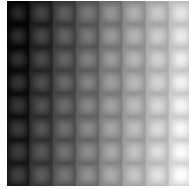
The height staggering we used for experiments has an $N_t = 9$ and $d_{\text{foci}} \approx 2d_0$. Although our simulations suggest that an N_t equal to or greater than 16 optimizes optical sectioning, we chose an

*All heights plotted linearly in gray scale

Jumping spiral



Raster



Diagonal

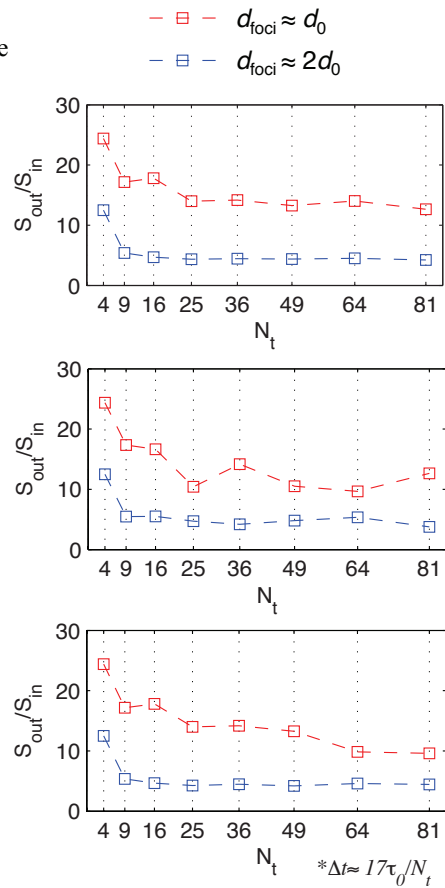
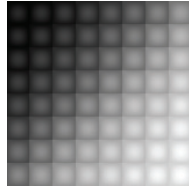


Figure 3.13: The ratios of out-of-focus signal to in-focus signal under three different spatial arrangements of distinct time-delay steps.

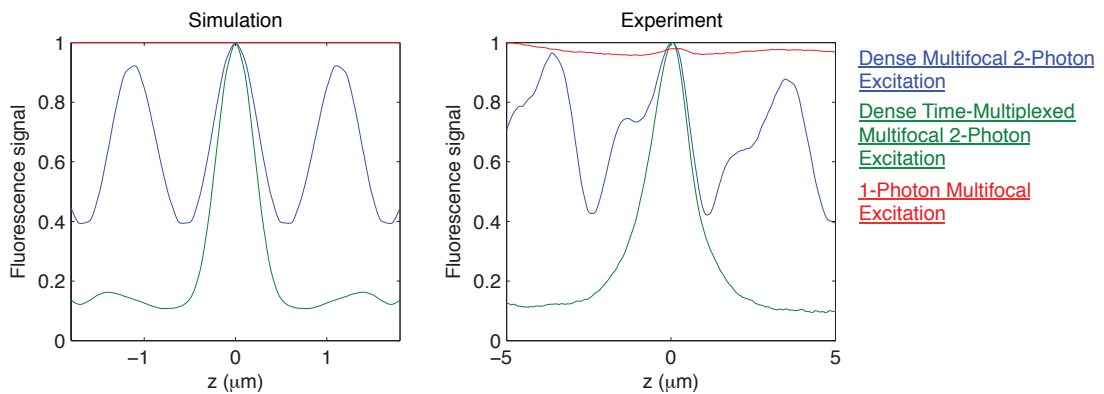


Figure 3.14: The numerically simulated and experimentally measured (excitation) axial responses of dense multifocal 2-photon excitation (blue), dense time-multiplexed multifocal 2-photon excitation (green), single-photon multifocal illumination (red). The interfocal distance $d_{\text{foci}} \approx 2d_0$ for both simulations and experiments. The height-staggering used for simulations and experiments has $N_t = 9$. The emission filter used for experiments has a transmission window at 554 ± 105 nm.

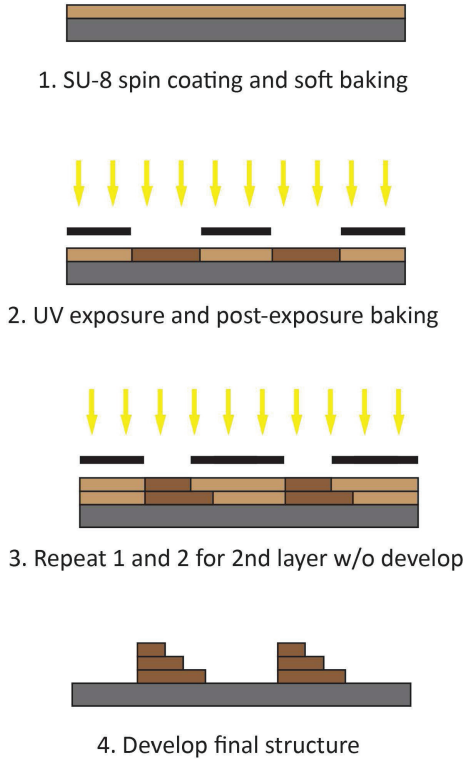


Figure 3.15: Illustration of the multi-exposure protocol we used to fabricate the height-staggered plate. The thickness of each SU-8 layer is $\sim 30 \mu\text{m}$.

$N_t = 9$ out of fabrication simplicity. After all, the results of simulations show that the improvement of optical sectioning by using $N_t = 16$ over $N_t = 9$ is around 10% in terms of the ratio of out-of-focus signal to in-focus signal, while making a 9-level height-staggering plate is nearly 2^7 times easier than a 16-level one. This is because the success of each repetitive procedure is independent of one another, but the failure of any single one means the failure of the entire fabrication. The fluorescent thin layer was made by sandwiching a tiny drop of a fluorescent dye between a #1.5 coverslip and a non-fluorescent quartz microscope slide (Ted Pella, Inc.). The fluorescent dye was diluted 3 times from a saturated 1,8-ANS solution of dimethylformamide. The thickness of the thin layer was estimated as $\leq 0.5 \mu\text{m}$ by dividing the volume of the dye drop with the coverslip area. In Fig. 3.14 the axial response of multifocal 2-photon excitation with only a microlens array is denoted as dense multifocal 2-photon excitation (blue line), while 2-photon excitation with a microlens array and height-staggered plate is denoted as dense time-multiplexed multifocal 2-photon excitation (green line). Although our usage of the height-staggered plate results from a context different from time

multiplexing of multifocal multiphoton microscopy, we named our technique so in order to credit it to the very first concept of introducing time multiplexing to reduce interfocal interferences at out-of-focus regions. The presented result of experiments are averaged out of 15 repeats.

Figure 3.14 shows qualitatively good agreement between the results of experiments and simulations. The quantitative difference between experiments and simulations is mostly caused by our usages of scalar field-based simulations rather than vectorial field-based ones.

3.2.5 Enhance optical sectioning by implementing structured illumination microscopy

As discussed in Section 3.2, our approach allows moderate out-of-focus excitation in order to keep d_{foci} small and image acquisition fast and simple. To further enhance the capability of optical sectioning of our technique, fortunately, the periodic multifocal pattern can be readily utilized for structured illumination microscopy, which can remove out-of-focus signal from acquired images. Here we demonstrate the optical performances of such implementation by numerical simulations as well as experimental measurements. Structured illumination microscopy relies on the post processing of multiple images, each noted as I_{img} . Because the emitted fluorescence (wavelength assumed to be $\sim 0.56\lambda_0$) from the specimen is generally incoherent, as discussed in Section 1.1, we can estimate I_{img} from a convolution of the excitation intensity profile I_{SP} and the intensity PSF of the microscopy system, I_{PSF} [20], as

$$I_{\text{img}}(\mathbf{r}') = \int I_{\text{SP}}(\mathbf{r}, z) f(\mathbf{r}, z) I_{\text{PSF}}(\mathbf{r}' + M\mathbf{r}, M^2z) d^2\mathbf{r} dz, \quad (3.27)$$

where f is the concentration distribution of the fluorophore in the specimen. To quantify the optical-sectioning effect, we assume that the specimen is an ideal thin fluorescent film placed at $z = z_f$, i.e., $f(\mathbf{r}, z) = \delta(z - z_f)$. eq. (3.27) then becomes

$$I_{\text{img}}(\mathbf{r}; z_f) = \int I_{\text{SP}}(\mathbf{r}', z_f) I_{\text{PSF}}(\mathbf{r} + M\mathbf{r}', M^2z_f) d^2\mathbf{r}'. \quad (3.28)$$

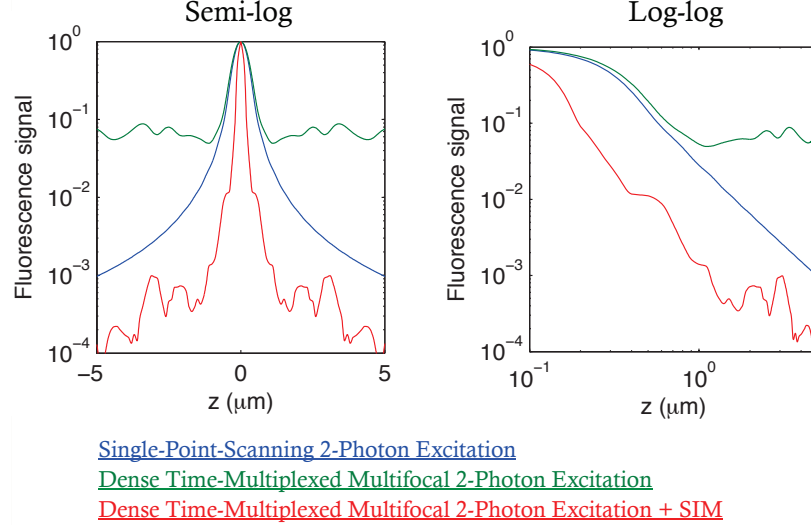


Figure 3.16: Simulated axial responses of single-point-scanning 2-photon excitation microscopy (blue), dense time-multiplexed multifocal multiphoton microscopy with (red) and without (green) structured illumination microscopy, in semi-log and log-log scales. The wavelength of the emitted fluorescence is set to be ~ 510 nm. $d_{\text{foci}} \approx 2d_0$.

Conventional structured illumination microscopy takes 3 shifts of the 1-dimension periodic pattern; each step is $1/3$ of the period of the pattern [3]. In our case, the periodicity of I_{SP} is 2-dimensional. We thus use 3-by-3 shifts ($I_{\text{img}1}, I_{\text{img}2}, \dots, I_{\text{img}9}$ denote the obtained images) and apply the post-processing routine of structured illumination microscopy to extract the optically sectioned images

$$I_{\text{SIM}} = \sqrt{\sum_{i=1}^9 \sum_{j=1}^9 (I_{\text{img}i} - I_{\text{img}j})^2}. \quad (3.29)$$

We then substitute I_{SP} in eq. (3.26) with I_{SIM} to evaluate the overall strength of optical sectioning (Fig. 3.16).

The results show that after applying structured illumination microscopy, we can reproduce the $1/z^2$ axial response as observed in single-point-scanning 2-photon excitation microscopy. From the results of simulations we also found that the axial resolution of our technique has a ~ 1.3 -fold improvement over that of a single-point-scanning confocal microscope (Fig. 3.17).

Although confocal microscopy is conventionally regarded as the standard technique for achieving diffraction-limited optical sectioning, we should note that this is not a fundamental breakthrough of diffraction limit. Similar performance can be expected if one implements structured illumination

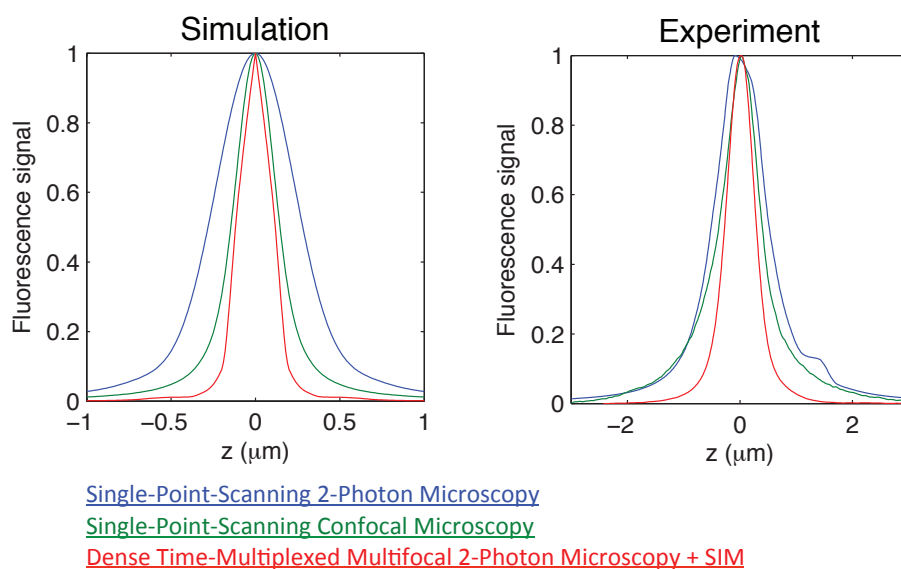


Figure 3.17: Comparisons of axial responses of single-point-scanning 2-photon microscopy (blue), single-point-scanning confocal microscopy (green) and dense time-multiplexed multifocal 2-photon microscopy in conjunction with structured illumination microscopy (red) in both numerical simulations and experiments. The simulated/experimental FWHMs of each techniques are $0.56/1.04 \mu\text{m}$ for single-point-scanning 2-photon microscopy, $0.29/0.79 \mu\text{m}$ for single-point-scanning confocal microscopy, and $0.24/0.56 \mu\text{m}$ for dense time-multiplexed multifocal 2-photon microscopy in conjunction with structured illumination microscopy. The wavelengths of excitation and emission in simulations of single-point-scanning confocal microscopy are both 510 nm . The emission filter used for experiments has a transmission window at $510 \pm 5 \text{ nm}$.

microscopy on conventional multifocal multiphoton microscopy or multifocal confocal microscopy, and such an improvement can be understood as a combination of two different, independent optical-sectioning mechanisms [37]. The advantage of implementing structured illumination microscopy on our system is simplicity. Combining structured illumination microscopy with multifocal multiphoton/confocal microscopy requires additional telescoping between the structured pattern and the spinning disk, which is by itself a complicated opto-mechanic device. On the contrary, performing structured illumination microscopy on our system requires only acquire individual image at each translation/scanning step, which can be easily edited into several microscope management software programs.

We further simulate the images of a virtual 3-dimensional object obtained by the different imaging techniques (Fig. 3.18) to illustrate the optical sectioning of our proposed dense time-multiplexed multifocal multiphoton microscopy in conjunction with structured illumination microscopy (denoted as dTMMMM + SIM). Compared with conventional epifluorescence microscopy (Fig. 3.18(b), Epi), the images obtained before structured-illumination post processing (denoted as dTMMMM) shows the ability of intrinsic optical sectioning. In the log-scale intensity plot (Fig. 3.18(c)), dTMMMM + SIM has the highest signal contrast between fluorescent and non-fluorescent areas, consistent with the results in Fig. 3.17. Moreover, the reconstructed 3-dimensional views show that dTMMMM + SIM successfully reproduces the details of the object (Fig. 3.18(d)).

To demonstrate the capability of imaging living biological systems, we also performed optical sectioning on living *C. elegans* using our proposed technique (Fig. 3.19, dTMMMM + SIM). In Fig. 3.19 we also compare the z -sequential images obtained under our technique and conventional epifluorescence microscopy. The imaged *C. elegans* on both microscopes have two mechanosensory neurons separated by $\sim 5 \mu\text{m}$ on z axis, and we can see that our technique shows clear axial segregation of the two neurons.

We should note that the post processing of structured illumination microscopy introduced here, i.e., the 9-frame imaging procedure and eq. (3.29), is not the only way to remove out-of-focus signal from the obtained images I_{img} . Other methods using a high-spatial-frequency illumination pattern

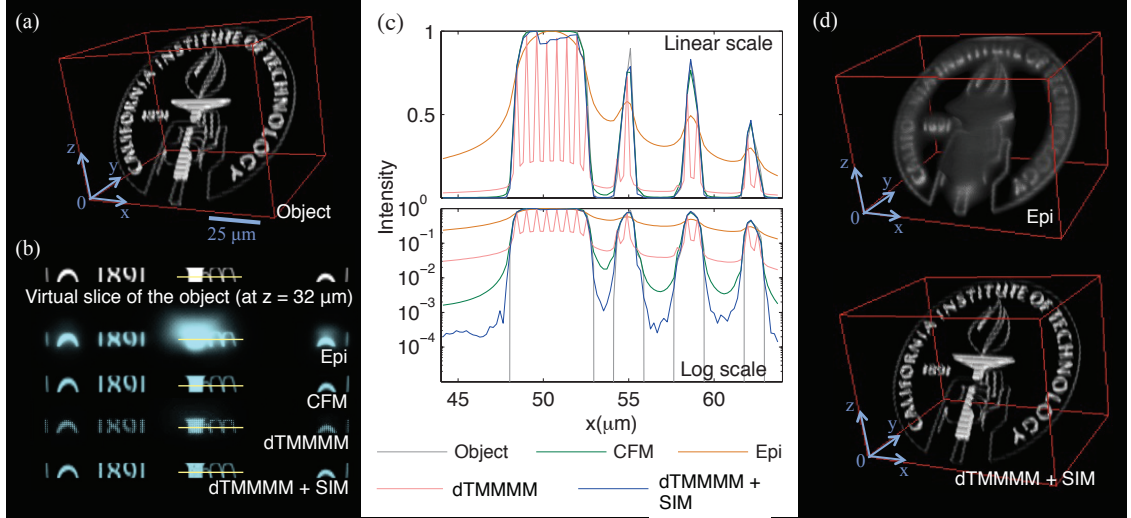


Figure 3.18: Image analysis of conventional epifluorescence microscopy (Epi), single-point-scanning confocal microscopy (CFM), dense time-multiplexed multifocal multiphoton microscopy with (dTMMMM + SIM) and without (dTMMMM) implementing structured illumination microscopy. (a) The object. (b) The simulated images obtained by various techniques at the corresponding depth of the virtual slice. The intensity profiles indicated by the yellow line segments are plotted in (c). (d) 3D-view reconstructed from the z-stacked images of Epi and dTMMMM + SIM.

to distinguish in-focus and out-of-focus signals, such as HiLo microscopy [38, 39], may also be applied to the proposed optical setup. These methods use different imaging procedures and post-processing algorithms, which may lead to different imaging properties such as acquisition speed and spatial resolutions, such that different methods may be most suitable for different imaging applications. For example, the HiLo method, whose algorithms are more complicated than eq. 3.29, requires only 2 frames to retrieve in-focus signal, one frame each with uniform and non-uniform illumination; the reduced number of frames may therefore shorten the imaging time. However, such an advantage exists only when the frame rate of the camera is much lower than the repetition rate of the ultrafast pulse train. If these two rates fall in the same order of magnitude, one will need to increase the acquisition time to shift the structural illumination pattern around the sample so as to mimic the effect of uniform illumination, and the overall imaging time will eventually be similar to conventional structured illumination microscopy.

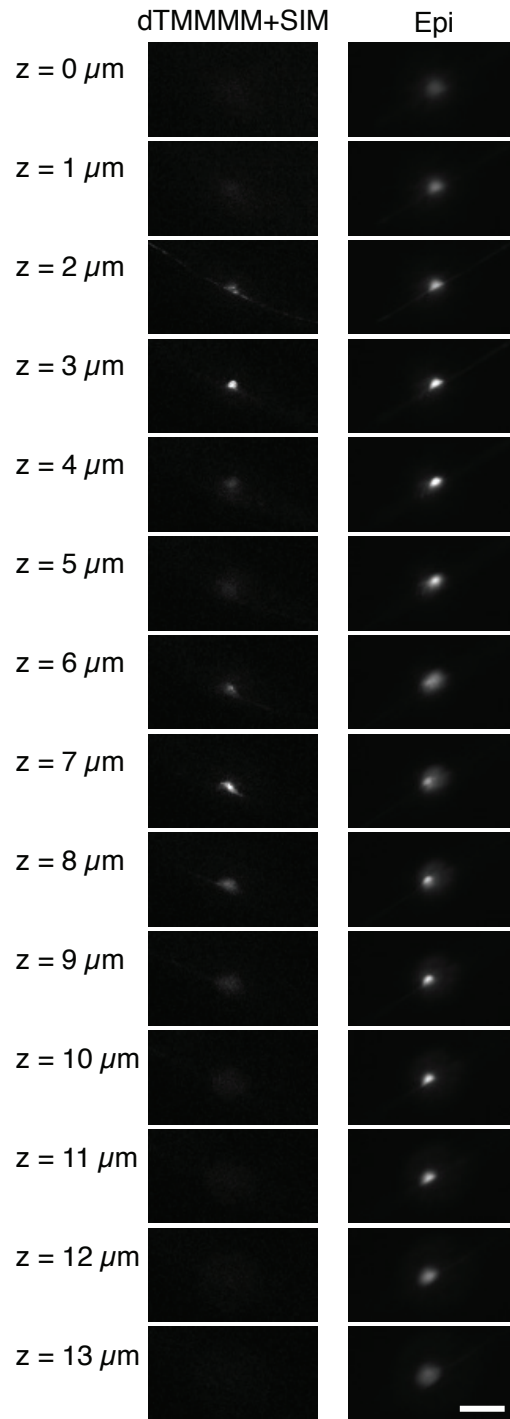


Figure 3.19: Images of sequential depths of *C. elegans* obtained under dense time-multiplexed multifocal multiphoton microscopy in conjunction with structured illumination microscopy (dTMMMM + SIM) and conventional epifluorescence microscopy (Epi). The imaged strain (ZDLS5) expresses green fluorescent protein in its mechanosensory neurons. Each translation/scanning step is exposed for 100 ms; 3-by-3 translation/scanning steps were used to construct a sectioning image. Scale bar: 20 μm .

3.2.6 Brief summary

Our numerical simulations and experiments shows that dTMMMM + SIM can provide optical sectioning by combining temporal focusing/time multiplexing and structured illumination in a simple optical setup, and achieves an axial resolution finer than single-point-scanning confocal microscopy. Our analysis provides the design guide of HSMAs with small time-delay increments; the dimensions of the proposed HSMAs are compatible with standard biomedical microscopes, and feasible for existing fabrication methods. In contrast to conventional structured illumination microscopy, the intrinsic sectioning of our method can reduce photobleaching and increase the signal-to-noise ratio of the processed images.

Compared with multifocal multiphoton/confocal microscopy, our technique has a denser spacing of foci (> 10 foci per 10^2 -focus area), and thus has greater potential in high-speed imaging. In addition to the fine axial resolutions, the lateral resolution of our technique can also be enhanced via utilization of the periodic excitation structures and Fourier analysis of the obtained images [40]. Moreover, our technique can use the pulse train generated by ultrafast amplifiers, thereby yielding a sufficient signal level and moderate impact on the specimen at high acquisition rates, as demonstrated in our previous diffuser-based temporal focusing setup [36]. Taken together, we have shown that dense time-multiplexed multifocal multiphoton microscopy in conjunction with structured illumination microscopy has the potential to achieve (better-than-conventional) diffraction-limited, high-frame-rate volumetric imaging with a simple, wide-field optical design.

3.3 High-degree time-multiplexed multifocal multiphoton microscopy by a length-staggered fiber bundle

As discussed in previous sections, our HSMA-based temporal focusing/time-multiplexing does not provide the standard $1/z^2$ axial response because of the moderate out-of-focus excitation. The only way to further reduce this out-of-focus excitation is to employ even larger total time delays Δt_{tot} . However, as we mentioned previously, it is not practical to use the conventional pillar-like

structures to create high-degree time multiplexing because of the nature of diffraction of light waves propagating in free space. Such diffraction leads to the divergence of a propagating beam, which can cause a leakage of light between neighboring pillars, thereby degrading temporal separation and optical sectioning. We show in the last section that such a divergence depends on the cross-sectional area of the pillars, and that having a negligible light leakage requires:

$$A \geq \lambda_0 \Delta h_{\max}, \quad (3.30)$$

where λ_0 is the central wavelength of the light pulse, A is the cross-sectional area of a single pillar and Δh_{\max} is the maximal height difference among the pillars. Using eq. (3.30) to estimate the dimensions of a time-multiplexing device that can perform scanningless wide-field imaging with an ~ 100 -fs duration ultrafast pulse train, we found that it requires Δh_{\max} to be > 30 mm and the cross-sectional area of the entire device to be larger than 100 cm^2 [37]. Fulfilling both of these requirements on one optical device is far beyond the fabrication capability of current optical-quality manufacturing techniques. Alternatively, this light leakage is avoidable if the ends of the pillars can be aligned on individual planes perpendicular to the optical axis of the imaging system, e.g., a conventional microlens array, which apparently provides no time multiplexing.

In this section we present a new design for a time-multiplexing device, one that can be easily manufactured and that creates a high degree of time multiplexing without the concerns of light leakage between neighboring time-delay channels. Our device consists of a bundle of optical fibers of various lengths, wherein time multiplexing is created by the relative length differences among the fibers. To avoid the aforementioned light leakage, we aligned the ends of all the fibers at the input and output planes, while the length differences were compensated by slight bending of the fibers (Fig. 3.20).

Because of the length differences of the optical fibers, input light pulses that simultaneously enter

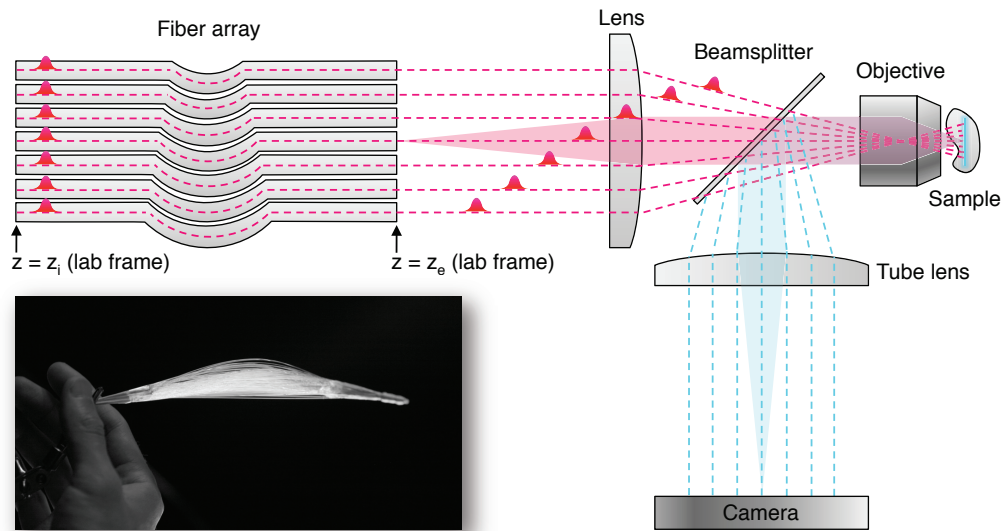


Figure 3.20: Schematic of the optical system. After a light pulse passes through the fiber bundle, multiple light pulses are generated with spatial and temporal separations amongst one another, and create a plane of foci at the focal plane of the microscope objective. Because of the temporal separation, the optical properties of each focus can be considered identical to the conventional single-focus multiphoton microscopy [5]. The fluorescence emitted within the excited plane are then collected by the microscope objective and routed to a camera for wide-field imaging. The dashed lines show the central traces of the light pulses passing through individual optical fibers, and the shaded region exemplifies the beam profile of a light pulse exiting an optical fiber. The inset is a photograph of the actual fiber bundle.

two fibers will exit the bundle with a temporal separation of:

$$\Delta t = \frac{n \Delta l}{c}, \quad (3.31)$$

where n is the refractive index of the fiber core, Δl is the length difference between the two fibers and c is the speed of light in vacuum. Previous studies suggested that having a temporal separation of twice of the pulse duration τ is sufficient to create time multiplexing between two foci [5], indicating that the minimal length difference between the two fibers should be:

$$\Delta l_{\min} = \frac{2\tau c}{n}. \quad (3.32)$$

This distance is $\sim 14 \mu\text{m}$ in our implementation, for which $\tau \approx 35 \text{ fs}$ and $n \approx 1.5$. Based on these estimates, we developed a fiber bundle prototype consisting of 168 optical fibers (see Section 3.3.1 for details). Specifically, we separated the fibers into 84 groups of different lengths, each of which contained 2 fibers that were meant to be cut into the same length, with the path difference between adjacent length groups of $\sim 200 \mu\text{m}$. Because of the limited precision of our fiber cutting method, there is a moderate length fluctuation within each fiber pair, which was measured to have a standard deviation of $\sim 30 \mu\text{m}$ (Fig. 3.21). Given $\Delta l_{\min} \approx 14 \mu\text{m}$, a statistical analysis (see Section 3.3.2 for details) showed that combining the designated inter-group length differences and the stochastic intra-group length fluctuation can lead to ~ 146 unique time delays, nearly 50 times higher than that achieved to date in conventional time-multiplexing devices [41]. To provide a straightforward coupling process with reasonable efficiency, we used large-core multimode fibers to assemble the prototype and butt-coupled the ultrafast light pulses into the bundle.

To examine whether the fiber bundle can prevent interfocal interaction and suppress out-of-focus excitation, we compared the axial response of our system with: 1) a non-time-multiplexed multifocal system that has foci spacing similar to that used here, and 2) single-point-scanning systems that, by design, have no interfocal interferences. Here, system 1 represents conventional multifocal multiphoton microscopy that uses a microlens array for illumination [4], while system 2 provides

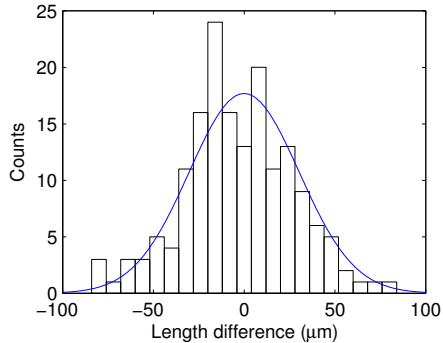


Figure 3.21: Length distribution of fibers that were meant to be cut into the same length. To quantify the length stochasticity induced by our fiber cutting procedures, we measured the lengths of 160 fibers that were prepared through the same procedures, and plot here the histogram of the differences between the measured lengths and the designated length. The distribution of length differences is in good agreement with a Gaussian distribution of a $30 \mu\text{m}$ standard deviation (blue line).

a quantitative comparison to conventional single-point-scanning multiphoton excitation microscopy [2]. The axial responses of each system were measured by imaging the same thin fluorescent layer at sequential depths around the focal plane of the microscope objective. To fairly compare the out-of-focus excitation of our time-multiplexed system and a non-time-multiplexed system, we chose a microlens array where the aperture formed by single microlens exhibited an axial-response FWHM (Fig. 3.22, red broken line) similar to that measured under single-fiber illumination (see Section 3.3.4 for details). The results show that the axial response of our fiber-bundle system resembles those of single-point-scanning systems illuminated with either a single microlens or an optical fiber (Fig. 3.22), and therefore confirm that the length differences of the fibers can indeed create sufficient temporal separations among the spatially neighboring foci to prevent out-of-focus excitation. Using multimode fibers, however, can create an axial response that is a mixture of the axial responses of several optical modes. As higher-order modes generally exhibit greater focal depths, such mode mixing should lead to a broader peak in the axial response curve. Indeed, the axial response curve measured in the system with single-fiber illumination showed a FWHM of $\sim 1.8 \mu\text{m}$ (Fig. 3.22, black broken line), in contrast with the $\sim 0.9\text{-}\mu\text{m}$ FWHM in an optimized conventional single-point-scanning multiphoton excitation microscope using the same objective [1].

To further demonstrate the fast optical-sectioning capability of our system, we imaged fluorescent

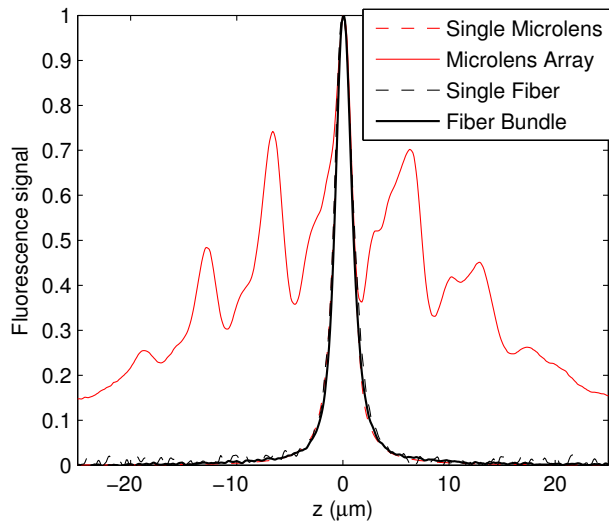


Figure 3.22: Comparison of axial response curves of multiphoton excitation with and without time multiplexing. The similarity of the axial responses of fiber-bundle (solid-black line) and single-fiber (broken-black line) illumination demonstrates that the length differences among the fibers can indeed create time multiplexing to prevent out-of-focus excitation, which is extensive in the non-time-multiplexed microlens-bundle illumination geometry (solid-red line).

microspheres embedded in agarose gel. For each optical section, we used four translational steps of the fiber bundle to homogenize the illumination field, with each step exposed for 1 millisecond, equivalent to an overall frame rate of 250 fps. Figure 3.23 shows both the three-dimensional visualization of the 15- μm -diameter microspheres and one section of the sample. Together, the results displayed in Fig. 3.22 and 3.23 demonstrate that the high degree of time multiplexing achieved by our fiber-bundle method can efficiently prevent out-of-focus excitation and thereby enable fast optical sectioning.

Having highlighted the advantages of our proposed technique, we now further discuss the technical features and limits of our system regarding: a) time multiplexing, b) imaging speed, c) imaging depth, and d) optical sectioning. First, without the physical constraints and manufacture difficulties associated with conventional time-multiplexing devices, the degree of time multiplexing of our system is limited only by relative group delays generated by different length fibers, which can lead to unequal excitation among the foci. With this regard, it can be shown that the number of unique time delays

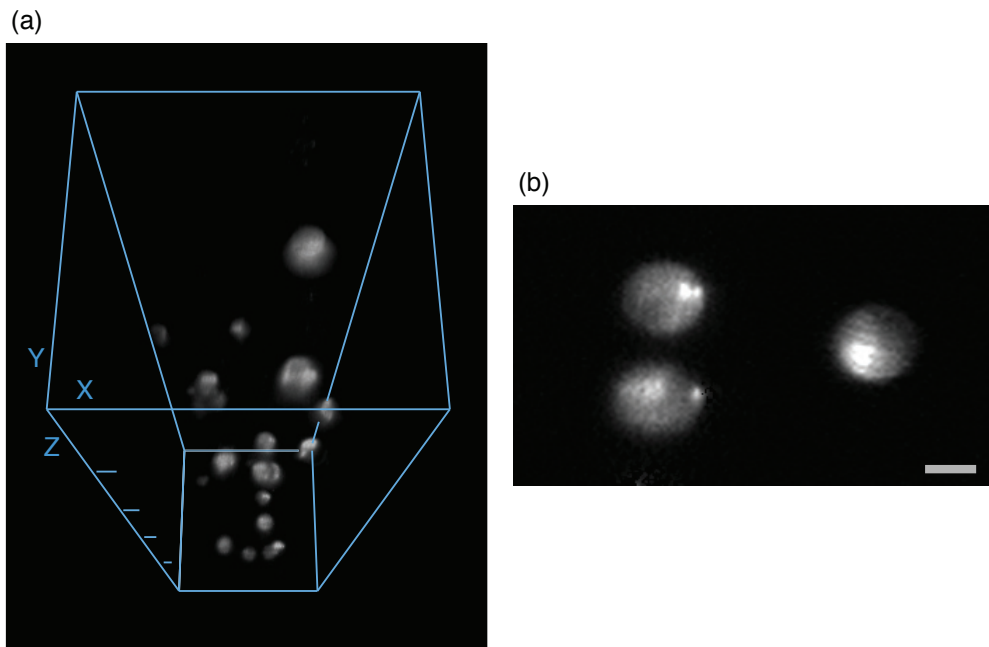


Figure 3.23: 3-dimensional reconstruction (a) and an optical section (b) of fluorescent microspheres embedded in agarose gel. We used 3D Viewer of ImageJ to reconstruct the 3-dimensional view from 332 sequential optical sections with a $3\text{-}\mu\text{m}$ depth interval. For each optical section, we integrated four images of 1-ms exposure obtained by translating the fiber bundle to four different positions, equivalent to an overall frame rate of 250 fps. The depth difference between adjacent Z ticks in (a) is $200\ \mu\text{m}$, and the scale bar in (b) is $10\ \mu\text{m}$. The microspheres are $15\ \mu\text{m}$ in diameter.

is bounded by:

$$N_{\text{TM}} \leq \left(\frac{n}{2\beta c |D|} \right) \cdot \tau, \quad (3.33)$$

where D is the dispersion parameter of the optical fiber, and β is the transformation constant of transform-limited light pulses (see Section 3.3.5 for details). In our system where $\tau \approx 35$ fs and $D \approx -116$ ps/nm/km, we obtained the upper bound of N_{TM} to be $\sim 1,500$, which is much larger than the aforementioned ~ 300 unique time delays required for scanningless imaging.

Second, for the speed of imaging, the instrumental limitations are the repetition rate of the ultrafast pulse train, the frame rate of the camera, and the translation rate of fiber bundle – if translation is required for homogeneous illumination (translation is not absolutely necessary for fiber bundles made of closely spaced, low numerical-aperture fibers). To date, commercially available ultrafast oscillators can provide repetition rates up to 1-10 GHz at average powers of over a Watt, while if larger single pulse energies are needed, regenerative amplifiers can produce \geq mJ pulses with repetition rates into the many tens of kHz. Scientific-grade CMOS cameras already exceed rates of 1,000 fps with limited numbers (~ 100 -by- 100) of pixels, and further advances in frame rate and image size can be expected. For fiber-bundle translation, fast mechanical stages typically achieve step rates of ~ 1 kHz; for even faster operation, galvanometric mirrors that translate the foci at rates higher than 50 kHz can be used, in an optical design similar to a previously demonstrated multifocal system [42]. Thus, the imaging speed of our technique can be pushed well beyond 1,000 fps even with the limits of currently available equipment and techniques.

Third, the imaging depth of our technique could be more significantly impaired by optical scattering and aberration induced by the sample compared with the non-imaging detection of conventional single-point-scanning multiphoton microscopy. This occurs because our technique, like SPIM and structured illumination microscopy, requires imaging the emitted light onto the sensor array of a camera. Such a disadvantage may be mitigated by spatial registration of the signal, i.e., assigning the signal collected by certain pixels of the sensor array to individual foci, and utilizing the spatial information associated with the foci to reconstruct the entire image [42]. One can also transform such a methodology into frequency registration of the signal, i.e., encoding the amplitudes of foci

with various frequencies and reconstructing the image through frequency analysis of the collected fluorescence signal [43]. In addition, if the fluorescence signal is strong enough, the scattering-induced blur can be numerically removed by applying structured illumination[3] using the foci pattern; this approach may also enhance the axial resolution [37, 44, 45].

Fourth, for the optical sectioning capability, the optimized axial resolution of our technique is equivalent to that of conventional single-point-scanning multiphoton excitation microscopy. Such an optimization requires the beam exiting the fiber to be collimated to the microscope objective with a flat wavefront and uniform amplitude distribution, suggesting that a single-mode fiber bundle assembly is highly preferred. Achieving efficient light coupling with such a single-mode-fiber bundle requires high-precision alignment and assembly of a light-coupling microlens array with the fiber-array bundle. Fortunately, the technology for this demanding task has recently become commercially available due to the fast-growing demands of highly parallel optical communication [46, 47].

In summary, we demonstrate a simple technique that has achieved the highest degree of time multiplexing ever demonstrated in multifocal multiphoton microscopy. We show that by introducing length differences within a bundle of optical fibers, the induced time multiplexing efficiently prevents the out-of-focus excitation even among densely spaced foci. Upon optimization, our technique will surpass currently available wide-field optical-sectioning fluorescence microscopies in terms of axial resolution and system simplicity, and achieve spatial resolutions equivalent to conventional single-point-scanning multiphoton excitation microscopy. With an imaging speed potentially beyond 1,000 fps, we believe that our technique will become a powerful imaging tool in future life science research. In following sections we describe certain technical details of our fiber bundle-illumination method.

3.3.1 Fiber bundle manufacturing

As described in the main text, we assembled the fiber bundle with large-core multimode fibers (core diameter $\approx 62.5 \mu\text{m}$ and cladding diameter $\approx 125 \mu\text{m}$, dispersion coefficient $\approx -116.4 \text{ ps/nm/km}$, YOFC[®]) of various lengths. To cut the optical fibers into designated lengths, we fixed fibers on a precision translational stage to adjust the lengths, and cut the fibers with a cleaver next to the

stage. When assembling the fibers, both ends of the bundle were aligned perpendicular to the optical axis, as shown in Fig. 3.20. The length differences were compensated by slightly bending the fibers – the optical bending loss is negligible due to the relatively short length differences ($\Delta l_{\max} \approx 17$ mm) compared with the average length of the fiber bundle (≈ 200 mm). After assembly, the physical strength of the fiber bundle was further enhanced by applying UV-cured epoxy near the ends of the fibers, followed by polishing and ultrasonic cleaning at both ends of the fiber bundle.

3.3.2 Statistical analysis of the degree of time multiplexing

To estimate the degree of time multiplexing created by our fiber preparation, we numerically simulated the length distribution of the resulting fiber bundle. As shown in Fig. 3.21, our fiber cutting method produced a Gaussian-like length distribution with a standard deviation of $\sim 30\text{-}\mu\text{m}$. To include such stochasticity, we added a Gaussian random variable with a mean at $0\ \mu\text{m}$ and a standard deviation of $30\ \mu\text{m}$ to the lengths of the fibers in each length group. We then compared the length differences among all 168 fibers in the bundle and determined the number of unique time delays. Specifically, we reduced 168 by the number of fibers that have a length difference less than Δl_{\min} with another fiber in the bundle to obtain the number of unique time delays (Δl_{\min} indicates the minimal length difference for creating two unique time delays, set to be $14\ \mu\text{m}$ in the simulation). By averaging 1,000 simulations we concluded that $\sim 146 \pm 4$ unique time delays can be produced by our fiber bundle preparation.

3.3.3 Development of the optical system

The light source of our system is a Ti:Sapphire ultrafast regenerative amplifier (Legend Elite-USP-1k-HE, Coherent, Inc.) seeded with an ultrafast oscillator (Mantis-5, Coherent, Inc.), and is butt-coupled into the fiber bundle. The repetition rate and pulse duration of the ultrafast pulse train are ~ 1 kHz and ~ 35 fs, respectively. In our infinity-corrected optical setup (Fig. 3.20), the output end of the fiber bundle was placed at the focal plane of the collimation lens ($f = 150$ mm plane-convex lens, KPX100AR.16, Newport Corp.). The temporally and spatially separated pulses entered an

inverted microscope frame (IX71, Olympus) through its back port, and were reflected upward to the microscope objectives by a beamsplitter (20RQ00UB.2 of customized dimensions, Newport Corp.). The emitted fluorescence then formed an image on the sensor array of an electron-multiplying CCD camera (iXon DU-885K, Andor). To measure the axial response shown in Fig. 3.22, we used a high numerical aperture oil-immersion lens (PlanApo N 60X NA 1.42, Olympus) equipped with a high-precision piezo stage (P-725 PIFOC[®], Physik Instrumente) for axial translation. The objective used for acquiring the optical sections shown in Fig. 3.23 is a long-working-distance water-immersion lens (XLUMPlanFL N 20X NA 1.00, Olympus). The number of translation steps for a homogeneous illumination field was estimated as the square of the ratio of foci spacing to foci diameter. In our system this ratio is ~ 2 , and thus we used a 2^2 -step translation to image each depth in the sample.

3.3.4 Measurement of axial responses

We measured the axial response by imaging a thin fluorescent layer with the microscope objective translated through 200 sequential depths at $0.3\text{-}\mu\text{m}$ intervals. The thin layer was made by sandwiching a tiny drop of a fluorescent dye between a #1.5 coverslip and a non-fluorescent quartz microscope slide (Ted Pella, Inc.). The fluorescent dye was diluted 3 times from a saturated 1,8-ANS solution of dimethylformamide. The thickness of the thin layer was estimated as $\leq 1\text{ }\mu\text{m}$ by dividing the volume of the dye drop with the coverslip area. To measure the axial response of the non-time-multiplexing microlens array, we replaced the fiber bundle with a square-microlens array (lens pitch $\approx 100\text{ }\mu\text{m}$, focal length $\approx 3\text{ mm}$, Flexible Optical B.V.) of foci spacing similar to our fiber bundle. To have a similar number of foci as those generated by our fiber bundle, we placed a mechanical iris in front of the microlens array to partially block the excitation beam.

We conducted the single-fiber illumination by placing a $50\text{ }\mu\text{m}$ pinhole (P50S, Thorlabs, Inc.) next to the input plane of the fiber bundle to selectively couple the excitation beam to a single fiber. Because of the geometry of the mechanical mount and the high filling factor of the microlens array, this pinhole-based technique required modest corrections to properly model a single-microlens illumination geometry. To obtain the proper axial response curve equivalent to that of single-

microlens illumination, we first applied geometric optics calculations to estimate the equivalent aperture formed by a single microlens, and then measured the axial response through a conventional single-focus multiphoton microscope with the equivalent aperture placed in front of the back aperture of the microscope objective. Each axial response curve was averaged from 15 separate z-scans.

3.3.5 Estimating the upper bound of the number of unique time delays

As described in the main text, the degree of time multiplexing of our technique is limited by the group velocity dispersion of the ultrafast pulses within the fibers. The relative group delays generated by different length fibers results in pulse duration variations in the exiting light pulses, which can lead to unequal excitation among the foci. To mitigate this effect, the overall group delay $\Delta\tau_{\text{GVD}}$ should be restricted such that:

$$\Delta\tau_{\text{GVD}} \approx \Delta l_{\text{max}} \cdot \Delta\lambda \cdot |D| \leq \tau, \quad (3.34)$$

where Δl_{max} is the maximal fiber length difference in the bundle, $\Delta\lambda$ is the spectral span of a transform-limited light pulse, and D is the dispersion parameter of the optical fiber. Under such a restriction, the brightest foci will be no more than twice as bright as the darkest ones. Given $\tau \approx \alpha/\Delta\lambda$ for transform-limited light pulses (β is a transformation constant), eqs. 3.32 and 3.34 suggest that the largest number of unique time delays is bounded by:

$$N_{\text{TM}} \approx \frac{\Delta l_{\text{max}}}{\Delta l_{\text{min}}} \leq \left(\frac{n}{2\beta c |D|} \right) \cdot \tau. \quad (3.35)$$

For commonly used near-infrared optical fibers and transform-limited Gaussian pulses, $\frac{n}{2\beta c |D|}$ is ~ 50 fs^{-1} at $\lambda_0 \approx 800$ nm. In our system where $\tau \approx 35$ fs and $D \approx -116$ ps/nm/km, we obtained that N_{TM} is upper-bounded by $\sim 1,500$.

Chapter 4

Discussions and Conclusions

4.1 Discussions

Table 4.1 compares existing wide-field optical-sectioning techniques with our innovated ones. As discussed in earlier chapters, conventional parallelization approaches using multifocal excitation improve imaging speed limitedly because the distances among foci must be large enough to prevent signal cross-talk among parallel channels. Further and for the same reason, the fast scanning of multifocal patterns typically relies on a spinning microlens-array disk, which is technically elaborative to manufacture. Multifocal confocal microscopy, in particular, requires precision alignment of a microlens-array disk and a pinhole-array disk. Structured illumination microscopy, although provides a fundamental breakthrough in terms of parallelization (and thus imaging speeds), sacrifices the dynamic range of the camera for unwanted out-of-focus signals and therefore leads to degraded signal-to-noise ratio of the processed images. The separation of illumination and detection paths makes SPIM uniquely suitable for imaging certain biological systems, but such an optical design comes at prices of compromised axial resolution and inconvenient sample handling. Temporal focusing microscopy generalized the concept of time multiplexing to provide gap-less illumination and optical sectioning at the same time. Nonetheless, its requirement of a high-order diffracted beam for generating time delays greatly limits its applicability of imaging multiple fluorophores in the one task.

Our innovated integration of dense time-multiplexed multifocal multiphoton microscopy and

structured illumination microscopy successfully overcomes the drawbacks of time-multiplexed multi-focal multiphoton microscopy, structured illumination microscopy and temporal focusing, and meanwhile retains their advantages. The minor issue of such integration is that the out-of-focus excitation remains at a moderate level, because the overall time delay is greatly limited by both the diffraction of electromagnetic waves and micro-optics fabrication techniques. These difficulties are successfully and fundamentally overcome by our novel design of the time-multiplexing device: a bundle of length-staggered optical fibers. In order to provide sufficient pulse energy for exciting fluorophores in the entire field of view at each pulse, our techniques require the usage of ultrafast amplifiers, which are relatively pricey compared with other components of a conventional wide-field microscope. In this regard, the ongoing innovations of fiber-based ultrafast amplifiers [48] can be expected to reduce the overall costs and greatly enhance the availability of our techniques. Also, as mentioned previously, the usages of low-repetition-rate amplified pulse trains can reduce light-induced photo-bleaching and thermal-mechanical damages [17, 30].

4.2 Conclusions

In the history of the development of optical imaging techniques, optical microscopy systems have been generally understood in a static manner, i.e., the optical properties of the microscopy systems can be fully analyzed in time-independent geometrical optics-based and/or physical optics-based models. In this thesis, we show that for multiphoton excitation fluorescence microscopy, there is still certain space for investigations and innovations in temporal aspects, and this space is not quite accessible if the dynamics of light pulses are over-simplified or even ignored as they usually were in previous studies. Specifically, we investigate the possibilities of using 0-order diffraction to generate time delays to reduce out-of-focus excitation in wide-field multiphoton excitation fluorescence microscopy. We discover the fundamental limitation, i.e., the inter-channel light leakage issue, of such a methodology, and develop a physical optics-based simulation to optimize the optical systems under this limitation. Furthermore, we also invent a new method, fiber-bundle illumination, to ultimately resolve this limitation.

Our methods, especially the fiber-bundle illumination technique, can be the most powerful optical-sectioning techniques among the existing ones upon optimization. It provides conceptually true scanningless illumination for high-frame-rate imaging, equivalent axial response to single-point-scanning multiphoton excitation fluorescence microscopy, extremely low (average) excitation intensity that is suitable for living-cell imaging, and at the same time its optical design is almost as simple as a conventional far-field optical microscope. Such simplicity makes the technique itself potentially low cost, easy to be used, maintained and even innovated by briefly trained persons. We can therefore expect this technique to trigger more and more exciting inventions, explorations and discoveries in various research fields such as fiber optics, bio-imaging, and ultimately, biology. I believe that our techniques can greatly increase the availability and user-friendliness of diffraction-limited volumetric fluorescence imaging techniques, and thus broadly benefit bio-imaging-related researches in the near future.

Table 4.1: Features of wide-field optical-sectioning techniques. Ratio of in-focus to out-of-focus excitation is estimated assuming that the microscope objective is a 60X NA 1.42 oil-immersion lens; the corresponding depth of field is $\sim 0.8 \mu\text{m}$ in the visible band. *Instrumentally achievable frame rates. **The width of field of view is assumed to be $100 \mu\text{m}$.

	System Simplicity	Frame Rate*	Ratio of In-Focus to Out-of-Focus Excitation	Specific Drawbacks
Multifocal Confocal Microscopy	Moderate	~ 500 fps or less	~ 3	Fixed pinhole size
(Time-Multiplexed) Multifocal Multiphoton Microscopy	Moderate	~ 500 fps or less	~ 3	
Structured Illumination Microscopy	High	$> 1,000$ fps	$\sim 1/25$	Degraded signal-to-noise ratio
Selective Plane Illumination Microscopy	Moderate	$> 1,000$ fps	$\sim 1/2^{**}$	Trade-off between axial resolution and width of field of view Inconvenient for sample handling
Temporal Focusing Microscopy	High	$> 1,000$ fps	$\sim 1/12$ [6]	Wavelength-dependent optical path Requires ultrafast amplifiers
Dense Time-Multiplexed Multifocal Multiphoton Microscopy + SIM	High	$> 1,000$ fps	$\sim 1/4$	Requires ultrafast amplifiers
Fiber Bundle-Based Time-Multiplexed Multifocal Multiphoton Microscopy	High	$> 1,000$ fps	~ 3	Requires ultrafast amplifiers

Bibliography

- [1] J. B. Pawley, *Handbook of biological confocal microscopy* (Springer, New York, NY, 2006), 3rd ed.
- [2] W. Denk, J. H. Strickler, and W. W. Webb, “Two-photon laser scanning fluorescence microscopy,” *Science* **248**, 73–6 (1990).
- [3] M. Neil, R. Juskaitis, and T. Wilson, “Method of obtaining optical sectioning by using structured light in a conventional microscope,” *Optics Letters* **22**, 1905–1907 (1997).
- [4] J. Bewersdorf, R. Pick, and S. Hell, “Multifocal multiphoton microscopy,” *Optics Letters* **23**, 655–657 (1998).
- [5] A. Egner and S. Hell, “Time multiplexing and parallelization in multifocal multiphoton microscopy,” *Journal of the Optical Society of America A-Optics Image Science and Vision* **17**, 1192–1201 (2000).
- [6] D. Oron, E. Tal, and Y. Silberberg, “Scanningless depth-resolved microscopy,” *Opt Express* **13**, 1468–76 (2005).
- [7] J. Huisken, J. Swoger, F. Del Bene, J. Wittbrodt, and E. Stelzer, “Optical sectioning deep inside live embryos by selective plane illumination microscopy,” *Science* **305**, 1007–1009 (2004).
- [8] N. T. Shaked, B. Katz, and J. Rosen, “Fluorescence multicolor hologram recorded by using a macrolens array,” *Opt Lett* **33**, 1461–3 (2008).
- [9] B. W. Schilling, T. C. Poon, G. Indebetouw, B. Storrie, K. Shinoda, Y. Suzuki, and M. H. Wu, “Three-dimensional holographic fluorescence microscopy,” *Opt Lett* **22**, 1506–8 (1997).

- [10] G. Indebetouw and W. Zhong, “Scanning holographic microscopy of three-dimensional fluorescent specimens,” *J Opt Soc Am A Opt Image Sci Vis* **23**, 1699–707 (2006).
- [11] G. Popescu, *Quantitative phase imaging of cells and tissues*, McGraw-Hill biophotonics (McGraw-Hill, New York, 2011).
- [12] F. Zernike, “Phase contrast, a new method for the microscopic observation of transparent objects,” *Physica* **9**, 686–698 (1942).
- [13] M. Ormö, A. B. Cubitt, K. Kallio, L. A. Gross, R. Y. Tsien, and S. J. Remington, “Crystal structure of the *aequorea victoria* green fluorescent protein,” *Science* **273**, 1392–5 (1996).
- [14] J. R. Lakowicz, H. Szmajcinski, K. Nowaczyk, K. W. Berndt, and M. Johnson, “Fluorescence lifetime imaging,” *Analytical Biochemistry* **202**, 316–30 (1992).
- [15] A. Periasamy and R. N. Day, “FRET imaging of pit-1 protein interactions in living cells,” *J Biomed Opt* **3**, 154–60 (1998).
- [16] S. Potter, “Vital imaging: Two photons are better than one,” *Current Biology* **6**, 1595–1598 (1996).
- [17] B. Masters, P. So, C. Buehler, N. Barry, J. Sutin, W. Mantulin, and E. Gratton, “Mitigating thermal mechanical damage potential during two-photon dermal imaging,” *Journal of Biomedical Optics* **9**, 1265–1270 (2004).
- [18] L. C. Martin, *The theory of the microscope* (American Elsevier Pub. Co, New York, 1966).
- [19] M. Born and E. Wolf, *Principles of optics: electromagnetic theory of propagation, interference and diffraction of light* (Cambridge University Press, Cambridge, UK, 1997), 6th ed.
- [20] T. Wilson, *Confocal microscopy* (Academic Press, 1990).
- [21] M. Cahalan, I. Parker, S. Wei, and M. Miller, “Two-photon tissue imaging: Seeing the immune system in a fresh light,” *Nature Reviews Immunology* **2**, 872–880 (2002).

- [22] T. Nielsen, M. Fricke, D. Hellweg, and P. Andresen, “High efficiency beam splitter for multifocal multiphoton microscopy,” *J Microsc* **201**, 368–76 (2001).
- [23] I. Akira, T. Takeo, I. Katsumi, S. Yumiko, K. Yasuhito, M. Kenta, A. Michio, and U. Isao, “High-speed confocal fluorescence microscopy using a nipkow scanner with microlenses for 3-d imaging of single fluorescent molecule in real time,” *Bioimages* **4**, 57–62 (1996-06).
- [24] J. Palero, S. I. C. O. Santos, D. Artigas, and P. Loza-Alvarez, “A simple scanless two-photon fluorescence microscope using selective plane illumination,” *Opt Express* **18**, 8491–8 (2010).
- [25] T. V. Truong, W. Supatto, D. S. Koos, J. M. Choi, and S. E. Fraser, “Deep and fast live imaging with two-photon scanned light-sheet microscopy,” *Nat Methods* **8**, 757–60 (2011).
- [26] Z. W. Zhao, R. Roy, J. C. M. Gebhardt, D. M. Suter, A. R. Chapman, and X. S. Xie, “Spatial organization of rna polymerase ii inside a mammalian cell nucleus revealed by reflected light-sheet superresolution microscopy,” *Proc Natl Acad Sci U S A* **111**, 681–6 (2014).
- [27] A. Egner, V. Andresen, and S. W. Hell, “Comparison of the axial resolution of practical nipkow-disk confocal fluorescence microscopy with that of multifocal multiphoton microscopy: theory and experiment,” *J Microsc* **206**, 24–32 (2002).
- [28] A. Weigel, D. Schild, and A. Zeug, “Resolution in the apotome and the confocal laser scanning microscope: comparison,” *J Biomed Opt* **14**, 014022 (2009).
- [29] A. Vaziri and C. V. Shank, “Ultrafast widefield optical sectioning microscopy by multifocal temporal focusing,” *Optics Express* **18**, 19645–19655 (2010).
- [30] G. Donnert, C. Eggeling, and S. W. Hell, “Major signal increase in fluorescence microscopy through dark-state relaxation,” *Nature Methods* **4**, 81–86 (2007).
- [31] J. Mertz, “Molecular photodynamics involved in multi-photon excitation fluorescence microscopy,” *European Physical Journal D* **3**, 53–66 (1998).
- [32] M. Duncan, J. Reintjes, and T. Manuccia, “Scanning coherent anti-stokes raman microscope,” *Optics Letters* **7**, 350–352 (1982).

- [33] C. W. Freudiger, W. Min, B. G. Saar, S. Lu, G. R. Holtom, C. He, J. C. Tsai, J. X. Kang, and X. S. Xie, “Label-free biomedical imaging with high sensitivity by stimulated raman scattering microscopy,” *Science* **322**, 1857–1861 (2008).
- [34] J. Jahns and K.-H. Brenner, *Microoptics: from technology to applications*, vol. v. 97 (Springer, New York, 2004).
- [35] E. Hecht, *Optics* (Addison-Wesley, Reading, Mass., 2002), 4th ed.
- [36] J.-Y. Yu, C.-H. Kuo, D. B. Holland, Y. Chen, M. Ouyang, G. A. Blake, R. Zadoyan, and C.-L. Guo, “Wide-field optical sectioning for live-tissue imaging by plane-projection multiphoton microscopy,” *Journal of Biomedical Optics* **16**, 116009 (2011).
- [37] J.-Y. Yu, D. B. Holland, G. A. Blake, and C.-L. Guo, “The wide-field optical sectioning of microlens array and structured illumination-based plane-projection multiphoton microscopy,” *Opt Express* **21**, 2097–109 (2013).
- [38] D. Lim, K. K. Chu, and J. Mertz, “Wide-field fluorescence sectioning with hybrid speckle and uniform-illumination microscopy,” *Opt Lett* **33**, 1819–21 (2008).
- [39] D. Lim, T. N. Ford, K. K. Chu, and J. Mertz, “Optically sectioned in vivo imaging with speckle illumination holo microscopy,” *J Biomed Opt* **16**, 016014 (2011).
- [40] R. Heintzmann and P. A. Benedetti, “High-resolution image reconstruction in fluorescence microscopy with patterned excitation,” *Applied Optics* **45**, 5037–5045 (2006).
- [41] V. Andresen, A. Egner, and S. Hell, “Time-multiplexed multifocal multiphoton microscope,” *Optics Letters* **26**, 75–77 (2001).
- [42] K. H. Kim, C. Buehler, K. Bahlmann, T. Ragan, W.-C. A. Lee, E. Nedivi, E. L. Heffer, S. Fantini, and P. T. C. So, “Multifocal multiphoton microscopy based on multianode photomultiplier tubes,” *Opt Express* **15**, 11658–78 (2007).
- [43] S. S. Howard, A. Straub, N. Horton, D. Kobat, and C. Xu, “Frequency multiplexed in vivo multiphoton phosphorescence lifetime microscopy,” *Nat Photonics* **7**, 33–37 (2013).

- [44] H. Choi, E. Y. S. Yew, B. Hallacoglu, S. Fantini, C. J. R. Sheppard, and P. T. C. So, “Improvement of axial resolution and contrast in temporally focused widefield two-photon microscopy with structured light illumination,” *Biomed Opt Express* **4**, 995–1005 (2013).
- [45] P. J. Keller, A. D. Schmidt, A. Santella, K. Khairy, Z. Bao, J. Wittbrodt, and E. H. K. Stelzer, “Fast, high-contrast imaging of animal development with scanned light sheet-based structured-illumination microscopy,” *Nature Methods* **7**, 637–U55 (2010).
- [46] M. Stark, G. Esser, A. Lamott, and M. Geiger, “Laser based micro alignment for fabrication of highly precise 2D fiber collimator arrays,” in “PHOTON PROCESSING IN MICROELECTRONICS AND PHOTONICS III,” , vol. 5339 of *PROCEEDINGS OF THE SOCIETY OF PHOTO-OPTICAL INSTRUMENTATION ENGINEERS (SPIE)*, Herman, PR and Fieret, J and Pique, A and Okada, T and Bachmann, FG and Hoving, W and Washio, K and Xu, X and Dubowski, JJ and Geohegan, DB and Trager, F, ed., SPIE (SPIE-INT SOC OPTICAL ENGINEERING, 1000 20TH ST, PO BOX 10, BELLINGHAM, WA 98227-0010 USA, 2004), vol. 5339 of *PROCEEDINGS OF THE SOCIETY OF PHOTO-OPTICAL INSTRUMENTATION ENGINEERS (SPIE)*, pp. 144–155. Conference on Photon Processing in Microelectronics and Photonics III, San Jose, CA, JAN 26-29, 2004.
- [47] P. Trinh, *2D fiber arrays*, Silicon Lightwave Technology, Inc., 9277 Research Drive, Irvine, CA 92618 (1999). Date of access: March 3rd, 2014.
- [48] T. Eidam, J. Rothhardt, F. Stutzki, F. Jansen, S. Hädrich, H. Carstens, C. Jauregui, J. Limpert, and A. Tünnermann, “Fiber chirped-pulse amplification system emitting 3.8 gw peak power,” *Opt Express* **19**, 255–60 (2011).